Vibrational relaxation beyond the linear damping limit in two-dimensional optical spectra of molecular aggregates

Václav Perlík, and František Šanda

Vibrational relaxation beyond the linear damping limit in two-dimensional optical spectra of molecular aggregates

Václav Perlík and František Šanda[a)]
Institute of Physics, Faculty of Mathematics and Physics, Charles University, Ke Karlovu 5, Prague 121 16, Czech Republic

We present a computational model for the spectra of molecular aggregates with signatures of vibronic progression. Vibronic dynamics is implemented by coupling the dynamics of Frenkel excitons with underdamped vibrations. Vibrational dynamics includes linear damping resulting in the exponential decay and quadratic damping inducing subexponential or power law relaxation and increasing vibrational decoherence as demonstrated on lineshapes of the absorption spectrum. Simulations of the third-order coherent response account for bath reorganization during excitonic transport, which allows us to study the line-shape evolution of cross peaks of 2D spectra. *Published by AIP Publishing.*
[http://dx.doi.org/10.1063/1.4999680]

I. INTRODUCTION

Recent developments of the ultrafast optical technology provided new insights into the microscopic dynamics of exciton transport through molecular aggregates. Novel nonlinear experiments, such as two-dimensional (2D) spectroscopies in visible domain,[1–3] resolved discrepancies arising between different experiments on the same molecular systems (e.g., often inconsistent estimates for intermolecular forces deduced from the absorption spectrum and from the pump-probe kinetics) and restored some older debates.

The role of the electronic and vibrational coherences in the electronic transport[4,5] and the differences between the Förster regime[6] and Redfield regime of transport[7] has been at the center of the ongoing debate. These new experiments on organic dyes,[8,9] light harvesters,[10] and artificial molecular aggregates[11] often revealed the important role of underdamped vibrations in electronic transport. In other cases, while the effect of underdamped vibrations on transport rates was found minor or moderate, the vibronic modulation of electronic transitions was a key ingredient for explaining beatings of 2D spectra.[12–14] At the same time, however, the simulations of the interplay of vibrational and electronic dynamics constitute a serious computational challenge that has been approached at the various levels of theory.[15]

Simulations of nonlinear coherent response and 2D spectra of transporting multichromophoric electronic systems were pioneered by Zhang *et al.*[16] Their algorithm is based on diagonalization of the Frenkel exciton Hamiltonian describing dynamics of electronic degrees of freedom[17–21] and partitioning vibrationally (or solvent) induced fluctuations of excitons into a diagonal part modifying eigenfrequencies and an off-diagonal part modifying eigenstates. The former part induces dephasing between excitons, the dynamics of which is responsible for lineshapes, and is usually accounted for by the second cumulant.[22] The latter results into the exciton transport, the dynamics of which is standardly described by using generalized master equations,[23] generically of the Redfield type, as the present algorithm is naturally perturbative in the electron-vibration coupling.

While authors differ in the choice of the specific transport formalism[24] (e.g., to reach the Förster regime) and in the way how the transport and the dephasing are combined into the 2D lineshapes, the general strategy of Zhang *et al.* became a widely accepted standard for aggregates counting from a few to tens of molecules. Alternatives are at hand for very large or very small systems. For extended aggregates, made of hundreds of constituents, lineshapes of individual excitons are neglected and complex dynamics of multiple coherences is eventually factorized into a quasiparticle picture.[25] In the opposite limit, explicit representations of fluctuations[26,27] can avoid approximate factorizations of dephasing and transport and the Förster-Redfield dilemma for sufficiently small systems. These alternative strategies and later refinements of the original methods were reviewed in Refs. 28–30.

The algorithm in Ref. 16 works satisfactorily, provided the vibrational modulation of excitons is broad in frequencies without sharp peaks in the spectrum. Sharp peaks signify strongly coupled underdamped vibrations of which complex interferences with exciton coherences go beyond the Redfield or Förster type of transport. A proper study of vibration-electronic entanglement requires the representation of some vibrations explicitly, i.e., to diagonalize relevant vibrational modes together with electronic degrees of freedom to get mixed exciton-vibrational (called vibronic) eigenstates and calculate transport dynamics among these vibronic states. While implementation is costly for extended aggregates, it is accessible for the small ones. After redefining the "system" space from excitonic to vibronic, the rest of the simulation strategy instituted by Ref. 16 can be largely maintained. Variants of the vibronic approach to 2D spectra have been employed by several authors.[31–38]

---

a)Electronic mail: sanda@karlov.mff.cuni.cz

We report a vibronic dynamical model affordable for simulations of small molecular aggregates with resolved vibrational structure. Our preliminary calculations addressed the vibronic kinetics of artificial carotenoid-purpurin dyad[11] and the natural lycopene-chlorophyll complex of Rs. molischianum[10] as they combined dimer or trimer excitonic dynamics with vibrational relaxation. Models of vibrations standardly assume exponential decay, which results from linear vibration to bath interaction. The present communication aims to allow for more general vibrational kinetics. The linear model is a relic of reduced descriptions of vibrations in excitonic models, where it allowed for substantial savings of numerical effort. With an explicit representation of vibronic coordinates, the nonlinear coupling can be introduced at moderate costs. We will demonstrate that this extension allows for the description of subexponential and power law relaxation reported in biological systems[39–41] and addressed by a variety of phenomenological descriptions.[42–48]

We next expand the calculations of kinetics into the complete machinery for calculating optical spectra, both linear and nonlinear. For the latter, some kind of factorization of dephasing and relaxation dynamics is always required for simulations along with ideas in Ref. 16. We adopted a simulation protocol, which allows phase acquisition to follow the relaxation pathways and to account for the eigenfrequency correlations between different periods of a 2D experiment, while remaining computationally feasible.

This paper is structured as follows. In Sec. II we introduce a model of vibronic aggregates. System degrees of freedom, i.e., excitons, and a limited number of underdamped vibrations are separated from a bath of overdamped vibrations. In Sec. III we introduce the system-bath interaction Hamiltonian. Dynamics include the electronic dephasing term and linear and nonlinear vibrational damping. Dephasing inducing diagonal (eigenfrequency) fluctuations is distinguished from transport inducing off-diagonal (eigenstate) fluctuations. In Sec. IV we specify the effect of the former and describe transport dynamics using the master equation. We demonstrate the effect of nonlinear damping by predicting the subexponential or power law dynamics of relaxation. In Sec. V we take care of dephasing and study their effects on absorption lineshapes. In Sec. VI we calculate the third-order optical response by an algorithm that follows the reorganization of bath modes during transport. The effects of nonlinear damping on the 2D spectra will be demonstrated. In Sec. VII we conclude.

II. VIBRONIC AGGREGATE

We consider the optical dynamics of molecular aggregates with significant vibronic structure. The electronic structure of each molecule (counted as $i = 1, 2, \ldots, N$) of the aggregate is modeled by a two-level chromophore (with ground g_i and excited e_i levels, exciton creation operator $\hat{A}_i^\dagger$, and transition frequency ϵ_i). To describe the third-order coherent response, only a handful of states of the composed electronic Hilbert space of aggregates are needed. The relevant part consists of a ground state $|\Pi_i g_i\rangle$, the manifold of one-exciton states where a single chromophore is excited $|e_k \Pi_{i \neq k} g_i\rangle = \hat{A}_k^\dagger |\Pi_i g_i\rangle$,

and the manifold of doubly excited states $|e_k e_l \Pi_{i \neq k,l} g_i\rangle = \hat{A}_k^\dagger \hat{A}_l^\dagger |\Pi_i g_i\rangle$. The exciton dynamics is described by the Frenkel exciton Hamiltonian

$$\hat{H}_e = \hbar \sum_i \epsilon_i \hat{A}_i^\dagger \hat{A}_i + \hbar \sum_{\substack{i,j \\ i \neq j}} J_{ij} \hat{A}_i^\dagger \hat{A}_j + \hbar \sum_{\substack{i,j \\ i \neq j}} \Xi_{ij} \hat{A}_i^\dagger \hat{A}_j^\dagger \hat{A}_i \hat{A}_j, \quad (1)$$

where intermolecular coupling $\hbar J_{ij}$ is usually approximated by dipole-dipole force[49] and evaluated by using *ab initio* quantum chemistry.[50] Shifts of exciton energies, when ith and jth molecules are simultaneously excited, shall be accounted by $\hbar \Xi_{ij}$.

Vibronic dynamics arise when certain, strongly coupled and underdamped, vibrations are included into the Hilbert space. Vibrations are assumed to be local, each of them is attached to some chromophore, and $\hat{q}_{i,z}$ ($\hat{p}_{i,z}$) is the coordinate (momentum) of the zth mode on the ith chromophore. We assume the electronic potential surface $U_{i,z}(\hat{q}_{i,z}) = \frac{1}{2} m_{i,z} \omega_{i,z}^2 (\hat{q}_{i,z} - d_{i,z} \hat{A}_i^\dagger \hat{A}_i)^2$ to be harmonic with respect to nuclear coordinates $q_{i,z}$, displaced by $d_{i,z}$ between the electronic ground and excited surface, where $\omega_{i,z}$ is the vibrational frequency, and $m_{i,z}$ is the effective mass.

The vibrational Hamiltonian $\hat{H}_v = \sum_{i,z} \frac{\hat{p}_{i,z}^2}{2m_{i,z}} + U_{i,z}(\hat{q}_{i,z})$ can be diagonalized as

$$\hat{H}_v = \sum_{i,z} \hbar \omega_{i,z} (\hat{V}_{i,z}^\dagger \hat{V}_{i,z} + 1/2), \quad (2)$$

where $\hat{V}_{i,z}^\dagger$ ($\hat{V}_{i,z}$) are creation (annihilation) operators,

$$\hat{V}_{i,z}^\dagger = \sqrt{\frac{m_{i,z}\omega_{i,z}}{2\hbar}} (\hat{q}_{i,z} - d_{i,z} \hat{A}_i^\dagger \hat{A}_i) - i \sqrt{\frac{1}{2m_{i,z}\omega_{i,z}\hbar}} \hat{p}_{i,z}, \quad (3)$$

defined so as to add a vibrational quantum on the ground or on the excited state surface.

Thus, local states are products of ground state electronic wavefunctions g_i with well-known wave functions of harmonic vibrations,

$$|g_i \Pi_z n_{i,z}\rangle = \prod_z \frac{1}{\sqrt{n_{i,z}!}} \left(\hat{V}_{i,z}^\dagger \right)^{n_{i,z}} |0_i\rangle |g_i\rangle, \quad (4)$$

and excited state electronic wavefunctions $|e_i\rangle$ with wave functions of displaced harmonic oscillators,

$$|e_i \Pi_z \tilde{n}_{i,z}\rangle = \prod_z \frac{1}{\sqrt{n_{i,z}!}} \left(\hat{V}_{i,z}^\dagger \right)^{n_{i,z}} |\tilde{0}_i\rangle |e_i\rangle, \quad (5)$$

where $|0_i\rangle$ is the vibrational ground state on the electronic ground state, and $|\tilde{0}_i\rangle$ is the (shifted) vibrational ground state on the electronic excited state surface.

Vibrons are complex electronic-vibrational excitations in the product Hilbert space composed of both the electronic and the vibrational degrees of freedom and defined by the system Hamiltonian

$$\hat{H}_S = \hat{H}_e + \hat{H}_v. \quad (6)$$

In the absence of coupling, $J_{ij} = 0$, Hamiltonian (6) is diagonal in the product basis $\otimes_i |\psi_i\rangle$, where $|\psi_i\rangle$ is some vector listed in Eq. (4) or Eq. (5), $|\psi_i\rangle \in \{|g_i \Pi_z n_{i,z}\rangle, |e_i \Pi_z \tilde{n}_{i,z}\rangle\}$. This basis is also a convenient starting point for numerical

implementations in a general situation with $J_{ij} \neq 0$. Indeed, the matrix elements of the coupling term in Eq. (1) are factorized into the Franck-Condon overlap integrals readily implemented along with the rest of the vibronic Hamiltonian (6) diagonal in that basis. Then, it is subjected to a standard routine for numerical diagonalization obtaining eigenstates $|\alpha\rangle$ and eigenfrequencies ε_α (hereafter indexed by Greek letters),

$$\hat{H}_S = \sum_\alpha \hbar \varepsilon_\alpha |\alpha\rangle \langle \alpha| . \tag{7}$$

Dynamics generated by Hamiltonian Eq. (6) conserves the number of electronic excitations. Thus, each electronic manifold can be diagonalized separately. On the electronic ground state, there is no resonant coupling, the eigenfunctions are direct products $|\Pi_{i,z} g_i n_{i,z}\rangle$ of ground state electronic wave functions and wave functions of harmonic oscillators introduced in Eq. (4). These states form the ground state manifold, hereafter denoted as $\mathbb{G}$. Corresponding eigenenergies are $\hbar \sum_{i,z} n_{i,z} \omega_{i,z}$. The diagonalization of the states with one electronic excitation is a complex task; eigenstates are always obtained by a numeric diagonalization of the corresponding block of the Hamiltonian. A set of these vibronic states forms the one-exciton manifold ($\mathbb{E}$). For two-exciton electronic manifold ($\mathbb{F}$), the diagonalization is different for dimers and for larger aggregates. In a special case of a dimer, eigenstates are direct products $|e_1 e_2 \Pi_z \tilde{n}_{1,z} \tilde{n}_{2,z}\rangle$ of doubly excited electronic wave functions and wave functions of displaced harmonic oscillators with eigenenergies $\hbar \epsilon_1 + \hbar \epsilon_2 + \hbar \Xi_{12} + \hbar \sum_z (n_{1,z} \omega_{1,z} + n_{2,z} \omega_{2,z})$. For larger aggregates, the diagonalization of the second manifold is again numerical. The third and higher excitation manifolds do not enter the calculation of the third-order response.[28]

Interaction with the probing laser fields, $E(t)$ will be treated in a dipole and in Condon approximations and will be described using the interaction Hamiltonian

$$\hat{H}_I(t) = -(\hat{\mu} + \hat{\mu}^\dagger)E(t), \tag{8}$$

where $\hat{\mu} = \sum_i \mu_i \hat{A}_i$. Here, μ_i is the transition dipole moment between the ground and the excited state of the ith molecule. Matrix elements

$$\mu_{\alpha\beta} \equiv \sum_i \mu_i \langle \alpha | \hat{A}_i | \beta \rangle ,$$

$$\mu_{\alpha\beta}^\dagger \equiv \sum_i \mu_i^* \langle \alpha | \hat{A}_i^\dagger | \beta \rangle$$

will be used hereafter. In the present paper, we neglect the tensorial structure of nonlinear response and consider dipole moments to be (anti-)parallel as in the most common aggregates. Generalization to arbitrary geometries is straightforward and is well described elsewhere.[51]

III. INTERACTION WITH BATH

All other weakly coupled and overdamped vibrations along with the solvent degrees of freedom shall be included into the bath and approximated by a set of harmonic oscillators with the Hamiltonian

$$\hat{H}_B = \sum_k \hbar \Omega_k \hat{B}_k^\dagger \hat{B}_k, \tag{9}$$

where Ω_k is the frequency of a k-bath mode, and $\hat{B}_k^\dagger$ and $\hat{B}_k$ are its creation and annihilation operators, respectively.

Vibrons are modulated through the coupling to the bath. The exciton-bath coupling

$$\hat{H}_E = \hbar \sum_{k,i} \Omega_k \iota_{k,i} \left(\hat{B}_k + \hat{B}_k^\dagger \right) \hat{A}_i^\dagger \hat{A}_i \tag{10}$$

is responsible for exciton dephasing. Modulation of the system vibrations will be represented by the linear and the quadratic vibration to bath coupling,

$$\hat{H}_L = \hbar \sum_{k,i,z} \Omega_k \kappa_{k,i,z} \left(\hat{B}_k + \hat{B}_k^\dagger \right) \left(\hat{V}_{i,z}^\dagger + \hat{V}_{i,z} \right), \tag{11}$$

$$\hat{H}_N = \hbar \sum_{k,i,z} \Omega_k \zeta_{k,i,z} \left(\hat{B}_k + \hat{B}_k^\dagger \right) \left\{ \left(\hat{V}_{i,z}^\dagger + \hat{V}_{i,z} \right)^2 - 1 \right\}, \tag{12}$$

respectively. The linear coupling term Eq. (11) is responsible for exponential relaxation, described as early as 1936 by Landau and Teller when modeling relaxation by collisions in gasses.[52,53] Expansion along Eq. (3) suggests that we correct for the displacement on the electronic excited state as

$$\hat{H}_L = \sum_{k,i,z} \Omega_k \kappa_{k,i,z} \sqrt{2\hbar m_{i,z} \omega_{i,z}} (\hat{B}_k + \hat{B}_k^\dagger)(\hat{q}_{i,z} - d_{i,z} \hat{A}_i^\dagger \hat{A}_i).$$

An alternative definition of coupling which neglects the displacement term $\propto d_{i,z} \hat{A}_i^\dagger \hat{A}_i$ is often used, but the change does not bring any principal consequences as such a displacement term can be absorbed into $\hat{H}_{SB,E}$ by the redefinition of coefficients $\iota_{k,i} \rightarrow \iota_{k,i} - \sum_z \kappa_{k,i,z} d_{i,z}$ in Eq. (10). Similarly, the subtraction of "1" in the last factor on the lhs of Eq. (12) can be omitted, only causing redefinition of zero energy. We choose a form where vibrational operators become normally ordered and quadratic coupling thus vanishes at the vibrational ground state.

The exciton dephasing and linear vibrational term constitute the standard spin-boson model of lineshapes. Without exciton transport, the decoherence dynamics of independent excitons can be exactly solved using closed expressions of the second cumulant[54] without the need to represent underdamped vibrations explicitly. In contrast, the nonlinear damping $\hat{H}_{SB,N}$ goes beyond the standard spin-boson model. It is responsible for subexponential vibrational relaxation and certain line-shape effects as will be demonstrated in Secs. IV–VI.

Following the strategy in Ref. 16, the interaction Hamiltonian $\hat{H}_{SB}$,

$$\hat{H}_{SB} = \hat{H}_E + \hat{H}_L + \hat{H}_N, \tag{13}$$

shall be transformed into an eigenbasis [Eq. (7)] and partitioned $\hat{H}_{SB} = \hat{H}_{SB}^D + \hat{H}_{SB}^O$ into the diagonal part $\hat{H}_{SB}^D$ representing eigenenergy fluctuations and the off-diagonal part $\hat{H}_{SB}^O$ representing eigenstate fluctuations. Their effect will be treated in Secs. IV and V separately.

IV. VIBRONIC TRANSPORT

The off-diagonal part of interaction Eq. (13) reads as

$$\hat{H}_{SB}^{O} = \hbar \sum_{\substack{\alpha\beta \\ \beta\neq\alpha}} \sum_{k,i} \Omega_k \left(\hat{B}_k (a_{\alpha\beta}^i \iota_{k,i} + \sum_z v_{\alpha\beta}^{i,z} \kappa_{k,i,z} + \sum_z w_{\alpha\beta}^{i,z} \zeta_{k,i,z}) + h.c. \right) |\alpha\rangle\langle\beta|, \quad (14)$$

where we defined matrices $a_{\alpha\beta}^i \equiv \langle\alpha|\hat{A}_i^\dagger \hat{A}_i|\beta\rangle$, $v_{\alpha\beta}^{i,z} \equiv \langle\alpha|\hat{V}_{i,z}^\dagger + \hat{V}_{i,z}|\beta\rangle$, $w_{\alpha\beta}^{i,z} \equiv \langle\alpha|(\hat{V}_{i,z}^\dagger + \hat{V}_{i,z})^2 - 1|\beta\rangle$.

Its dynamical effect will be accounted for by using the master equation

$$\frac{d}{dt}\rho_{\nu\mu} = -i(\varepsilon_\nu - \varepsilon_\mu)\rho_{\nu\mu} - \sum_{\delta\beta} R_{\nu\mu,\delta\beta}\rho_{\delta\beta}, \quad (15)$$

where $\rho_{\nu\mu} \equiv \mathrm{Tr}\{|\mu\rangle\langle\nu|\hat{\rho}\}$ is the reduced (system) density matrix in the space of vibrons, and $R_{\nu\mu,\delta\beta}$ stands for a relaxation matrix. As argued by Redfield,[7] only certain terms called secular and obeying

$$\varepsilon_\nu - \varepsilon_\mu - \varepsilon_\delta + \varepsilon_\beta = 0 \quad (16)$$

contribute significantly to the time evolution of the density matrix. For aggregates, the eigenfrequencies are not systematically built so that Eq. (16) can only be obeyed when the exciton indices are properly paired. For $\mu = \nu, \delta = \beta$ pairing, i.e., $\varepsilon_\mu = \varepsilon_\nu, \varepsilon_\delta = \varepsilon_\beta$, the matrix element $R_{\nu\nu,\delta\delta}$ describes the population transport from state δ to state ν. Similarly for $\nu = \delta, \mu = \beta$ pairing, the matrix element $R_{\nu\mu,\nu\mu}$ describes the decay of coherence between states μ and ν. We adopt this secular approximation by introducing its characteristic function, $K_{\nu\mu\delta\beta} \equiv (1 - \delta_{\nu\delta})\delta_{\nu\mu}\delta_{\delta\beta} + \delta_{\nu\delta}\delta_{\mu\beta}$, and neglecting coherence transfers, coherence to transfer terms, etc. In addition to Redfield's argumentation based on relevance, secular dynamics preserves positive semidefiniteness of density matrices[55] and significantly reduces the number of Feynman diagrams involved in calculations in Sec. VI.

The relaxation matrix shall be evaluated to the second order in system-bath coupling $\hat{H}_{SB}^O$, following Refs. 56 and 57,

$$R_{\nu\mu,\delta\beta} = K_{\nu\mu\delta\beta} \, \mathrm{Tr}\{|\delta\rangle\hat{\rho}_B\langle\beta|$$
$$\times \int_0^\infty d\tau \, e^{-i\check{L}_0\tau}\check{P}\check{L}e^{i\check{Q}\check{L}_0\tau}\check{Q}\check{L}(|\mu\rangle\langle\nu|)\}, \quad (17)$$

where we used the following superoperator notation $\check{L}\cdot \equiv \frac{1}{\hbar}[\hat{H}_S + \hat{H}_{SB}^O + \hat{H}_B, \cdot]$, $\check{L}_0\cdot \equiv \frac{1}{\hbar}[\hat{H}_S + \hat{H}_B, \cdot]$, $\check{Q} = 1 - \check{P}$, and where the Argyres-Kelly projector[58] $\check{P}\cdot \equiv \sum_{\alpha,\gamma}|\alpha\rangle\langle\gamma|\,\mathrm{Tr}\{|\gamma\rangle\hat{\rho}_B\langle\alpha|\cdot\}$ accounts for the canonical bath density matrix

$$\hat{\rho}_B = \frac{e^{-\hat{H}_B/(k_BT)}}{\mathrm{Tr}_B\{e^{-\hat{H}_B/(k_BT)}\}} \quad (18)$$

at temperature T. We next evaluate Eq. (17). The rate constant for transport is ($\delta \neq \nu$)

$$R_{\nu\nu,\delta\delta} = -2 \sum_i a_{\nu\delta}^i a_{\delta\nu}^i \left[(1 + \mathcal{N}(\varepsilon_\delta - \varepsilon_\nu))\mathcal{A}_i(\varepsilon_\delta - \varepsilon_\nu)\right.$$
$$\left. + \mathcal{N}(\varepsilon_\nu - \varepsilon_\delta)\mathcal{A}_i(\varepsilon_\nu - \varepsilon_\delta)\right]$$
$$-2 \sum_{i,z} v_{\nu\delta}^{i,z} v_{\delta\nu}^{i,z} \left[(1 + \mathcal{N}(\varepsilon_\delta - \varepsilon_\nu))\mathcal{V}_{i,z}(\varepsilon_\delta - \varepsilon_\nu)\right.$$
$$\left. + \mathcal{N}(\varepsilon_\nu - \varepsilon_\delta)\mathcal{V}_{i,z}(\varepsilon_\nu - \varepsilon_\delta)\right]$$
$$-2 \sum_{i,z} w_{\nu\delta}^{i,z} w_{\delta\nu}^{i,z} \left[(1 + \mathcal{N}(\varepsilon_\delta - \varepsilon_\nu))\mathcal{W}_{i,z}(\varepsilon_\delta - \varepsilon_\nu)\right.$$
$$\left. + \mathcal{N}(\varepsilon_\nu - \varepsilon_\delta)\mathcal{W}_{i,z}(\varepsilon_\nu - \varepsilon_\delta)\right], \quad (19)$$

where $\mathcal{N}(x) = 1/(e^{\hbar x/(k_BT)}-1)$ is the Bose-Einstein distribution and where we defined

$$\mathcal{A}_i(x) \equiv \sum_k \Omega_k^2 \iota_{k,i}\iota_{k,i}\delta(x - \Omega_k),$$
$$\mathcal{V}_{i,z}(x) \equiv \sum_k \Omega_k^2 \kappa_{k,i,z}\kappa_{k,i,z}\delta(x - \Omega_k), \quad (20)$$
$$\mathcal{W}_{i,z}(x) \equiv \sum_k \Omega_k^2 \zeta_{k,i,z}\zeta_{k,i,z}\delta(x - \Omega_k)$$

as spectral densities relevant for exciton, linear vibration, and quadratic vibration to bath couplings, respectively. In Eq. (19) we have assumed that the three couplings are statistically independent and thus neglected cross terms $\propto \kappa\iota, \iota\zeta, \kappa\zeta$. Similarly we assumed that the various vibrations and chromophores are modulated independently. The generalization to arbitrary correlations is summarized in Appendix A.

The total rate for transport from state ν,

$$R_{\nu\nu,\nu\nu} = -\sum_{\substack{\delta \\ \delta\neq\nu}} R_{\delta\delta,\nu\nu}, \quad (21)$$

and the decoherence rates $\mu \neq \nu$,

$$R_{\nu\mu,\nu\mu} = \left[R_{\nu\nu,\nu\nu} + R_{\mu\mu,\mu\mu}\right]/2, \quad (22)$$

are derived from rates of Eq. (19). Spectral densities Eq. (20) are positive functions, e.g., $\mathcal{A}(x) \geq 0$, defined for positive frequencies $x > 0$. The successful estimation of spectral densities from microscopic foundations, e.g., molecular dynamical simulations, is rare.[59] In practice there are a handful of popular forms for spectral densities which are parameterized from experiments. In the simulation below, we use spectral densities of overdamped Brownian oscillator,[60]

$$\mathcal{A}_i(x) = \frac{2\lambda_{\mathcal{A}}^i \Lambda_{\mathcal{A}}^i x}{x^2 + (\Lambda_{\mathcal{A}}^i)^2}\Theta(x), \quad (23)$$

and the same forms for $\mathcal{V}_{i,z}$ and $\mathcal{W}_{i,z}$, where $\Lambda_{\mathcal{A}}^{i,z}$ is a bath relaxation rate, $\lambda_{\mathcal{A}}^{i,z}$ is a reorganization energy, and $\Theta(x)$ denotes the Heaviside step function.

We next examine the effects of the quadratic coupling Eq. (12) on master equation (15). To that end, we look into the purely vibrational relaxation (no electronic dynamics) of a
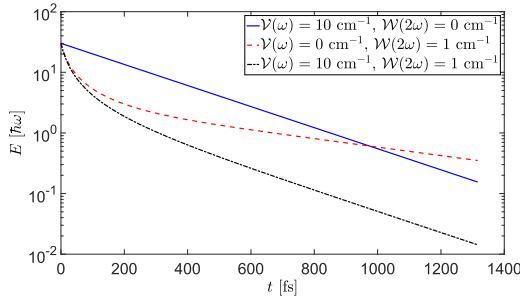
FIG. 1. Vibrational relaxation [Eq. (24)] in the log-linear plot. Comparison of exponential energy decay of linear damping [Eq. (11)] case (blue solid line) with power law energy relaxation of quadratic damping Eq. (12) (red dashed line). Their combination interpolate between short time power law and asymptotic exponential relaxation (black dotted-dashed line). Parameters inset, initial vibrational state $n = 30$.

single mode at low temperatures $\mathcal{N}(\omega) \to 0$. In the eigenbasis [Eq. (4)], the master equation (15) for populations

$$\frac{d\rho_{nn}}{dt} = 2\mathcal{W}(2\omega)\{(n+1)(n+2)\rho_{n+2\ n+2} - n(n-1)\rho_{nn}\}$$
$$+ 2\mathcal{V}(\omega)\{(n+1)\rho_{n+1\ n+1} - n\rho_{nn}\} \qquad (24)$$

shows the rates representing the linear $\propto \mathcal{V}(\omega)$ and quadratic damping $\propto \mathcal{W}(2\omega)$. The system of equations (24) was solved numerically, starting at $t = 0$ from the highly excited ($n = 30$) vibrational level. The decay of vibrational energy $\langle E \rangle \equiv \text{Tr}(\hat{H}_v - \frac{\hbar\omega}{2})\hat{\rho} = \hbar\omega \sum_n \rho_{nn}$ plotted by the dashed line in Fig. 1 manifests two regimes: Subexponential decay in the early times (higher excited levels) is controlled by quadratic terms $\propto \mathcal{W}(2\omega)$ in Eq. (24), as evident from comparison with the dashed line of limiting $\mathcal{V}(\omega) = 0$ solution. And exponential decay in the late times (low levels) is driven by the linear terms $\propto \mathcal{V}(\omega)$, sharing asymptotics with the dotted-dashed line of $\mathcal{V}(2\omega) = 0$ solution.

This behavior can be clarified from analytic considerations. Master equation (24) can be transformed into the evolution equation for the energy,

$$\frac{d\langle E \rangle}{dt} = -2\mathcal{V}(\omega)\langle E \rangle - \frac{4\mathcal{W}(2\omega)}{\hbar\omega}\langle E^2 \rangle, \qquad (25)$$

where we defined $\langle E^2 \rangle \equiv \sum_n n(n-1)(\hbar\omega)^2\rho_{nn}$. The linear damping represented by the first term on the rhs of Eq. (25) thus yields exactly exponential Landau-Teller decay [when the quadratic term is neglected $\mathcal{W}(2\omega) = 0$] as represented by the straight solid line in Fig. 1. With the second, quadratic term, Eq. (25) is not closed and cannot be solved simultaneously exactly and analytically. However, when closing it by approximating $\langle E^2 \rangle \approx \langle E \rangle^2$, we obtain the solution

$$\langle E \rangle(t) = \frac{\hbar\omega\mathcal{V}(\omega)}{2\mathcal{W}(2\omega)} \frac{1}{\left[1 + \frac{\hbar\omega\mathcal{V}(\omega)}{2\mathcal{W}(2\omega)\langle E \rangle(0)}\right]e^{2\mathcal{V}(\omega)t} - 1},$$

which interpolates between power law decay at early times $t < 1/\mathcal{V}(\omega)$,

$$\langle E \rangle(t) = \frac{\langle E \rangle(0)}{1 + t\left[\frac{4\langle E \rangle(0)\mathcal{W}(2\omega)}{\hbar\omega} + 2\mathcal{V}(\omega)\right]}, \qquad (26)$$

and switches to asymptotic exponential decay $\langle E \rangle(t) = e^{-2\mathcal{V}(\omega)t}\langle E \rangle(0)$ in an excellent agreement with numerics of Fig. 1. Note that power law in Eq. (26) is also an analytical solution for the $\mathcal{V}(\omega) = 0$ limiting case.

V. VIBRONIC LINESHAPES

We next describe the eigenfrequency ε_α fluctuations represented by the bath-space operator

$$\hat{\Delta}_\alpha \equiv \frac{1}{\hbar}\langle\alpha|\hat{H}_{SB}|\alpha\rangle$$

$$= \sum_{k,i} \Omega_k\hat{B}_k\left(a^i_{\alpha\alpha}\iota_{k,i} + \sum_z v^{i,z}_{\alpha\alpha}\kappa_{k,i,z} + \sum_z w^{i,z}_{\alpha\alpha}\zeta_{k,i,z}\right) + \text{h.c.}$$
$$(27)$$

Fluctuations given by Eq. (27) are linear in the bath coordinate $\hat{B}$ and thus represents Gaussian fluctuations, the treatment of which is standard and summarized below.

Gaussian fluctuations are fully characterized in terms of the matrix of correlation functions

$$C_{\beta\alpha}(t) \equiv \left\langle e^{i\hat{H}_Bt/\hbar}\hat{\Delta}_\beta e^{-i\hat{H}_Bt/\hbar}\hat{\Delta}_\alpha\right\rangle_B, \qquad (28)$$

where $\langle\hat{X}\rangle_B \equiv Tr_B\{\hat{X}\hat{\rho}_B\}$ with equilibrium bath density $\hat{\rho}_B$ defined in Eq. (18). Inserting Eq. (27) into Eq. (28) and expressing in terms of spectral densities Eq. (20) yield

$$C_{\beta\alpha}(t) = \frac{1}{2\pi}\int_{-\infty}^{\infty} d\omega \cos(\omega t)\coth\left(\frac{\hbar\omega}{2k_BT}\right)C''_{\beta\alpha}(\omega)$$
$$- \frac{i}{2\pi}\int_{-\infty}^{\infty}\sin(\omega t)C''_{\beta\alpha}(\omega), \qquad (29)$$

where

$$C''_{\beta\alpha}(\omega) = \sum_i a^i_{\alpha\alpha}a^i_{\beta\beta}\left[\mathcal{A}_{i,z}(\omega) - \mathcal{A}_{i,z}(-\omega)\right]$$
$$+ \sum_{z,i} v^{i,z}_{\alpha\alpha}v^{i,z}_{\beta\beta}\left[\mathcal{V}_{i,z}(\omega) - \mathcal{V}_{i,z}(-\omega)\right]$$
$$+ \sum_{z,i} w^{i,z}_{\alpha\alpha}w^{i,z}_{\beta\beta}\left[\mathcal{W}_{i,z}(\omega) - \mathcal{W}_{i,z}(-\omega)\right]. \qquad (30)$$

The effect of Gaussian noise on lineshapes is given by the line-shape function $g_{\beta\alpha}(t)$ obtained by the double integration of $C_{\beta\alpha}(t)$,

$$g_{\beta\alpha}(t) = \int_0^t d\tau \int_0^\tau d\tau' C_{\beta\alpha}(\tau'). \qquad (31)$$

Equation (31) can be used for arbitrary spectral densities, including the correlated ones, following the prescription in Appendix A. For the overdamped spectral densities in Eq. (23), these integrations can be carried over into the closed expressions summarized in Appendix B.

These functions are pivotal for determining lineshapes of the optical spectrum. The general algorithm for calculating the absorption of molecular aggregates will be presented in Sec. VI [see Eqs. (38) and (43)]. Here we clarify the effect of the three couplings of Eq. (13). We thus analyze absorption spectra for the two-level electronic chromophore with a single vibrational mode at low temperatures where Eq. (38) simplifies to

$$I(\Omega) = \sum_{\tilde{n}} |\mu_{0\tilde{n}}|^2 \int_0^\infty dt e^{i\Omega t}e^{-i(\epsilon + \tilde{n}\omega)t - R_{\tilde{n}0,\tilde{n}0}t}e^{-g_{\tilde{n}\tilde{n}}(t)}. \qquad (32)$$

Here the summation runs over vibrational states of the excited electronic manifold [Eq. (5)], and the dephasing rates $R_{\tilde{n}0,\tilde{n}0} = \tilde{n}\mathcal{V}(\omega) + \tilde{n}(\tilde{n} - 1)\mathcal{W}(2\omega)$ are half of transport rates of
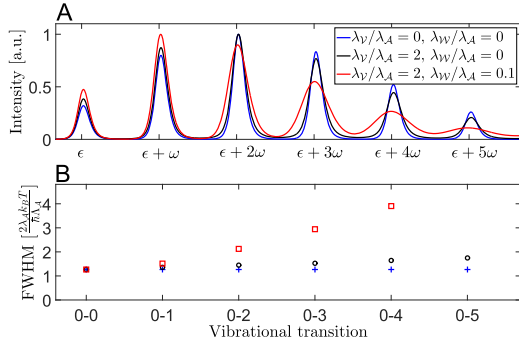
FIG. 2. Top panel: Effect of couplings (10)–(12) on the absorption lineshape of a single exciton with vibronic progression and pure excitonic dephasing ($\hat{H}_{SB,E}$) (blue line), linear coupling $\hat{H}_{SB,E} + \hat{H}_{SB,L}$ (black line), and quadratic coupling $\hat{H}_{SB,E} + \hat{H}_{SB,L} + \hat{H}_{SB,N}$ (red line). Bottom panel: FWHM of the peaks of vibronic progression. Parameters: $\frac{m\omega^2 d^2}{4\hbar\omega} = 1.25$, $\frac{\hbar\omega}{k_B T} = 5$, $\Lambda_{\mathcal{A}} = \Lambda_{\mathcal{V}} = \Lambda_{\mathcal{W}}$, $\omega/\Lambda_{\mathcal{A}} = 15$, $\lambda_{\mathcal{A}}/\Lambda_{\mathcal{A}} = 1$.

Eq. (24). Normally, the broadening induced by the R rates is minor and the line-shaping is mostly determined by the $g_{\tilde{n}\tilde{n}}$ functions.

Figure 2 shows the example spectra of the two-level chromophore with vibrational progression (top panel) and full width at half maximum (FWHM) for each peak (bottom panel). Pure electronic dephasing [Eq. (10)] shows a constant FWHM for all peaks of vibronic progression (blue line). The linear coupling [Eq. (11)] does not contribute to the line-shape function g as $v_{\tilde{n}\tilde{n}} = 0$ and the FWHM is only weakly growing with $\tilde{n}$ through the R rates (black line). In contrast, the quadratic coupling [Eq. (12)] with $g_{\tilde{n}\tilde{n}} \propto w_{\tilde{n}\tilde{n}}^2 \propto \tilde{n}^2$ results in progressively broadened peaks (red line) interpolating between linear $\propto \tilde{n}$ scaling of the FWHM for Gaussian lineshapes of slow limit $\lambda_{\mathcal{W}}/\Lambda_{\mathcal{W}} \to \infty$ and quadratic $\propto \tilde{n}^2$ scaling for Lorentzian lineshapes of fast limit $\lambda_{\mathcal{W}}/\Lambda_{\mathcal{W}} \to 0$ [see Eqs. (8.60b) and (8.60c) in Ref. 54]. Note that the transport and line-shape effects are carried by various parts of expansion $(V^\dagger + V)^2 = V^\dagger V^\dagger + V^\dagger V$ + h.c. The $\propto V^\dagger V^\dagger$ part is solely responsible for the vibrational decay shown in Fig. 1 and makes a very little contribution to lineshapes (through R), which is instead dominated by the $\propto V^\dagger V$ part. In conclusion, the quadratic coupling is capable of describing the increasing linewidth of peaks along the vibronic progression.

VI. PATHWAYS OF LINEAR AND NONLINEAR RESPONSE

In the present section, we shall combine results of Secs. IV and V into a general algorithm for the calculation of optical response. We switch formally into the Liouville space[54] and denote superoperators operating on ket (e.g., $\breve{\mu}^{(L)}\hat{X} = \hat{\mu}\hat{X}$) and operating on bra ($\breve{\mu}^{(R)}\hat{X} = \hat{X}\hat{\mu}$) indices of the density matrix by superscripts (L) and (R), respectively.

Optical response is usually expanded in powers of electric fields. Most experiments are related to the linear or the third-order response. Weak-field absorption is a Fourier transformation

$$S(\Omega) = \text{Re} \int_0^\infty e^{i\Omega t} S_L(t) dt \tag{33}$$

of the linear response function

$$S_L(t) = \text{Tr}\{\hat{\mu}\breve{G}(t)\breve{\mu}^{\dagger(L)}\hat{\rho}_{eq}\}, \tag{34}$$

where $\breve{G}(t) \equiv e^{-i\breve{H}^{(L)}t/\hbar} e^{i\breve{H}^{(R)}t/\hbar}$ is the evolution superoperator generated by the full Hamiltonian $\hat{H} = \hat{H}_S + \hat{H}_B + \hat{H}_{SB}$ and $\hat{\rho}_{eq}$ is the equilibrium density matrix.

A handful of experimental methods belonging to third-order spectroscopies such as time-resolved fluorescence, pump probe, transient grating, and 2D spectroscopy are represented by combinations of the following eight third-order response functions:

$$S_1(t_1, t_2, t_3) = \text{Tr}\{\hat{\mu}\breve{G}(t_3)\breve{\mu}^{\dagger(R)}\breve{G}(t_2)\breve{\mu}^{(R)}\breve{G}(t_1)\breve{\mu}^{\dagger(L)}\hat{\rho}_{eq}\},$$

$$S_2(t_1, t_2, t_3) = \text{Tr}\{\hat{\mu}\breve{G}(t_3)\breve{\mu}^{\dagger(R)}\breve{G}(t_2)\breve{\mu}^{\dagger(L)}\breve{G}(t_1)\breve{\mu}^{(R)}\hat{\rho}_{eq}\},$$

$$S_3(t_1, t_2, t_3) = \text{Tr}\{\hat{\mu}\breve{G}(t_3)\breve{\mu}^{\dagger(L)}\breve{G}(t_2)\breve{\mu}^{(L)}\breve{G}(t_1)\breve{\mu}^{\dagger(L)}\hat{\rho}_{eq}\},$$

$$S_4(t_1, t_2, t_3) = \text{Tr}\{\hat{\mu}\breve{G}(t_3)\breve{\mu}^{\dagger(L)}\breve{G}(t_2)\breve{\mu}^{\dagger(R)}\breve{G}(t_1)\breve{\mu}^{(R)}\hat{\rho}_{eq}\},$$

$$S_5(t_1, t_2, t_3) = -\text{Tr}\{\hat{\mu}\breve{G}(t_3)\breve{\mu}^{\dagger(L)}\breve{G}(t_2)\breve{\mu}^{(R)}\breve{G}(t_1)\breve{\mu}^{\dagger(L)}\hat{\rho}_{eq}\},$$

$$S_6(t_1, t_2, t_3) = -\text{Tr}\{\hat{\mu}\breve{G}(t_3)\breve{\mu}^{\dagger(R)}\breve{G}(t_2)\breve{\mu}^{(L)}\breve{G}(t_1)\breve{\mu}^{(R)}\hat{\rho}_{eq}\},$$

$$S_7(t_1, t_2, t_3) = -\text{Tr}\{\hat{\mu}\breve{G}(t_3)\breve{\mu}^{(L)}\breve{G}(t_2)\breve{\mu}^{\dagger(L)}\breve{G}(t_1)\breve{\mu}^{\dagger(L)}\hat{\rho}_{eq}\},$$

$$S_8(t_1, t_2, t_3) = \text{Tr}\{\hat{\mu}\breve{G}(t_3)\breve{\mu}^{(R)}\breve{G}(t_2)\breve{\mu}^{\dagger(L)}\breve{G}(t_1)\breve{\mu}^{\dagger(L)}\hat{\rho}_{eq}\}. \tag{35}$$

Their usual frequency domains are defined for nonrephasing diagrams $n = 1, 3, 5$ as

$$S_n(\Omega_1, t_2, \Omega_3) = \int_0^\infty \int_0^\infty dt_1 dt_3 e^{i\Omega_3 t_3 + i\Omega_1 t_1} S_n(t_1, t_2, t_3),$$

for rephasing diagrams $n = 2, 4, 6$ as

$$S_n(\Omega_1, t_2, \Omega_3) = \int_0^\infty \int_0^\infty dt_1 dt_3 e^{i\Omega_3 t_3 - i\Omega_1 t_1} S_n(t_1, t_2, t_3),$$

and for $n = 7, 8$ as

$$S_n(t_1, \Omega_2, \Omega_3) = \int_0^\infty \int_0^\infty dt_2 dt_3 e^{i\Omega_3 t_3 + i\Omega_2 t_2} S_n(t_1, t_2, t_3).$$

The usual representation of Eqs. (35) by double sided Feynman diagrams is shown in Fig. 3. Diagrams 1 and 2 represent photon emission, diagrams 3 and 4 represent ground state bleach, diagrams 5 and 6 represent excited state absorption (ESA), and diagrams 7 and 8 represent double quantum coherence signals.

Expressions (34) and (35) are still rather formal since the evolution superoperator $\breve{G}$ must include both the master equation and the dynamics of diagonal fluctuations and their combination is a complex task, which always requires approximations. To that end, we shall introduce $\mathcal{G}$, Green's function of master equation (15), and the operator $\mathcal{U}_\alpha(t) \equiv \langle \alpha | e^{-\frac{i}{\hbar}(\hat{H}_{SB}^D + \hat{H}_B)t} | \alpha \rangle$ for bath evolution when the system is in the α eigenstate. In the secular approximation, a coherence element of the density matrix is not mixed with other coherences or populations. Bath evolution is thus associated with fixed eigenstates and estimated without controversy as

$$G_{\alpha\beta,\alpha\beta}(t) = \mathcal{G}_{\alpha\beta,\alpha\beta}(t)\mathcal{U}_\alpha^L(t)\mathcal{U}_\beta^{\dagger R}(t). \tag{36}$$

Population elements of the density matrix are subject to transfers, and bath evolution is associated with various system eigenstates during time. Its accounting is thus complex, and applicable strategies range from (standard) complete neglect
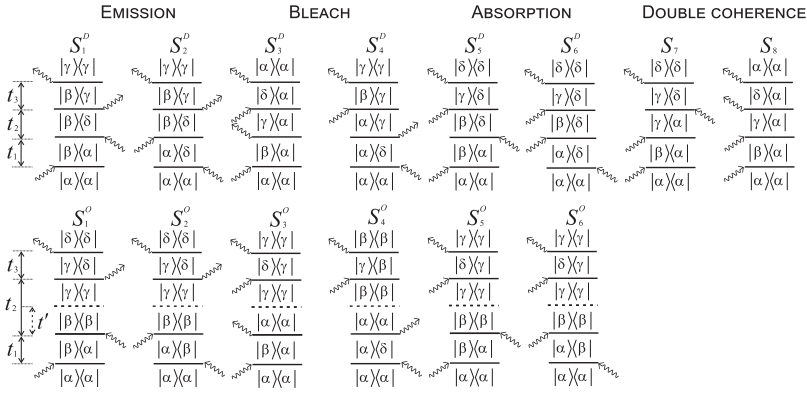
FIG. 3. Feynman diagrams (Liouville space pathways) for the third-order response functions, Eqs. (48) and (C1).

of the bath evolution $G_{\alpha\alpha,\gamma\gamma} = \mathcal{G}_{\alpha\alpha,\gamma\gamma}$, and thus neglect of the associated Stokes shift and lineshapes dynamics, over assumptions of bath evolution in some fixed system state and time scale separation arguments[61] to attempts to follow the jumps to some extent. Here, we followed the latter approaches and supplemented the system Green's function element $\mathcal{G}_{\alpha\alpha,\gamma\gamma}$, describing transfer from the initial state γ to the final state α, with bath evolution associated with the first part of time interval t' with γ and with final state α for the remaining time,

$$G_{\alpha\alpha,\gamma\gamma}(t) = \mathcal{G}_{\alpha\alpha,\gamma\gamma}(t)\mathcal{U}_\alpha^L(t-t')\mathcal{U}_\alpha^{\dagger R}(t-t')\mathcal{U}_\gamma^L(t')\mathcal{U}_\gamma^{\dagger R}(t'). \quad (37)$$

We thus allow for Stokes shift and 2D line-shape dynamics, and keeping $0 \ll t' \ll t$, Eq. (37) correctly reproduces both their static and fast fluctuation limits, surpassing approximations fixing the bath evolution in a certain state. For very simple systems, the interval t' can be even sampled from 0 to t in the spirit of Refs. 11 and 62 and such calculation could even be exact for unidirectional transports;[63,64] however, the numerical costs grow substantially then, beyond the applicability to vibronic aggregates. In the simulations shown in Figs. 4–6, we pick a simple choice $t' = t/2$. Sophistication of the best choice for t' is left for future research; the present approach is nevertheless computationally feasible and reproduces important limits. Note that the element $G_{\alpha\alpha,\alpha\alpha}(t) = \mathcal{G}_{\alpha\alpha,\alpha\alpha}(t)\mathcal{U}_\alpha^L(t)\mathcal{U}_\alpha^{\dagger R}(t)$ can be correctly subsumed to either Eq. (36) or Eq. (37). Elements of $\mathcal{G}$ not listed in Eqs. (36) and (37) vanish in the secular approximation, so we set $\mathcal{G}_{\alpha\beta,\gamma\delta}(t) = 0$ for them.

Combining Eq. (34) with Eq. (36), we get for the linear response function

$$S_L(t) = \sum_{\alpha\in\mathbb{G}}\sum_{\beta\in\mathbb{E}} \mu_{\alpha\beta}\mathcal{G}_{\beta\alpha,\beta\alpha}(t)\mu_{\beta\alpha}^\dagger \rho_{\text{eq},\alpha}F_{\alpha\beta}^{(2)}(t,0), \quad (38)$$

where $\rho_{\text{eq},\alpha} \equiv \text{Tr}_B\{\langle\alpha|\hat\rho_{\text{eq}}|\alpha\rangle\}$, and we merged the bath phase factor into

$$F_{\beta\alpha}^{(2)}(\tau_2,\tau_1) \equiv \text{Tr}_B\{\,\mathcal{U}_\alpha(0-\tau_2)\mathcal{U}_\beta(\tau_2-\tau_1)$$
$$\times \mathcal{U}_\alpha(\tau_1-0)\langle\alpha|\hat\rho_{\text{eq}}|\alpha\rangle\}/\rho_{\text{eq},\alpha}. \quad (39)$$

Here, it is assumed that the process starts at chromophore's electronic ground state with vibrations and bath populated according to the Boltzmann distribution of $\hat H_v + \hat H_{SB} + \hat H_B$. The equilibrium density matrix $\hat\rho_{\text{eq}}$ can be obtained by switching on the interaction $\hat H_{SB}$ at time $\tau = -\infty$ where we start from the uncorrelated density matrix $\hat\rho(-\infty)$ $\equiv \frac{e^{-\hat H_v/(k_B T)}}{\text{Tr}_v\{e^{-\hat H_v/(k_B T)}\}}|\Pi_i g_i\rangle\langle\Pi_i g_i| \otimes \hat\rho_B.$[65] Approximating $-\infty < \tau < 0$ evolution $\mathcal{U}(t) \equiv e^{-\frac{i}{\hbar}(\hat H_{SB}+\hat H_B)t}$ by neglecting transport $\langle\alpha|\mathcal{U}(t)|\alpha\rangle \approx \mathcal{U}_\alpha(t)$, we get

$$\hat\rho_{\text{eq}} \approx \sum_{\alpha\in\mathbb{G}} \rho_{\text{eq},\alpha}\mathcal{U}_\alpha(0+\infty)|\alpha\rangle\langle\alpha| \otimes \hat\rho_B\mathcal{U}_\alpha^\dagger(0+\infty), \quad (40)$$

where the equilibrium for vibrational ground states reads as

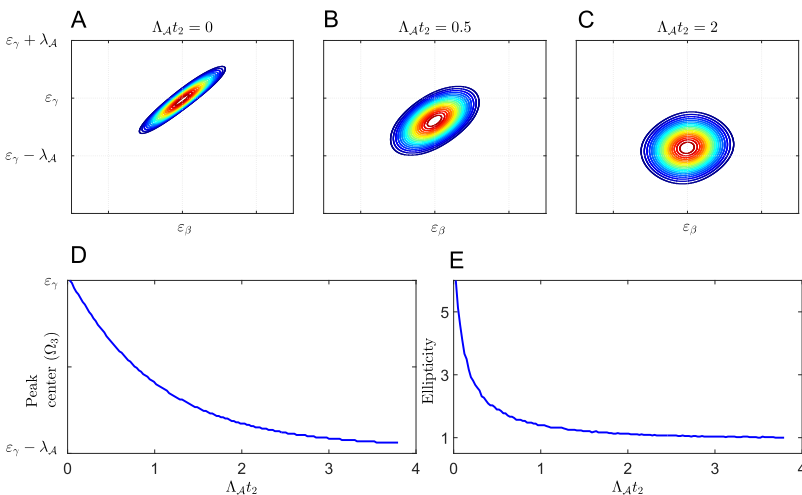FIG. 4. Top: 2D peak shapes of transport emission pathways $\text{Re}(S_1^O + S_2^O)$ at delays $\Lambda_\mathcal{A}t_2 = 0$ (a), $\Lambda_\mathcal{A}t_2 = 0.5$ (b), $\Lambda_\mathcal{A}t_2 = 2.0$ (c). Parameters $\varepsilon_\gamma - \varepsilon_\beta = \lambda_\mathcal{A} = 200\Lambda_\mathcal{A}$ $= \frac{10}{3}k_B T/\hbar$. Bottom: Stokes shift (d) and ellipticity (e) defined as the ratio of diagonal and anti-diagonal FWHM of the peak as a function of delay time.
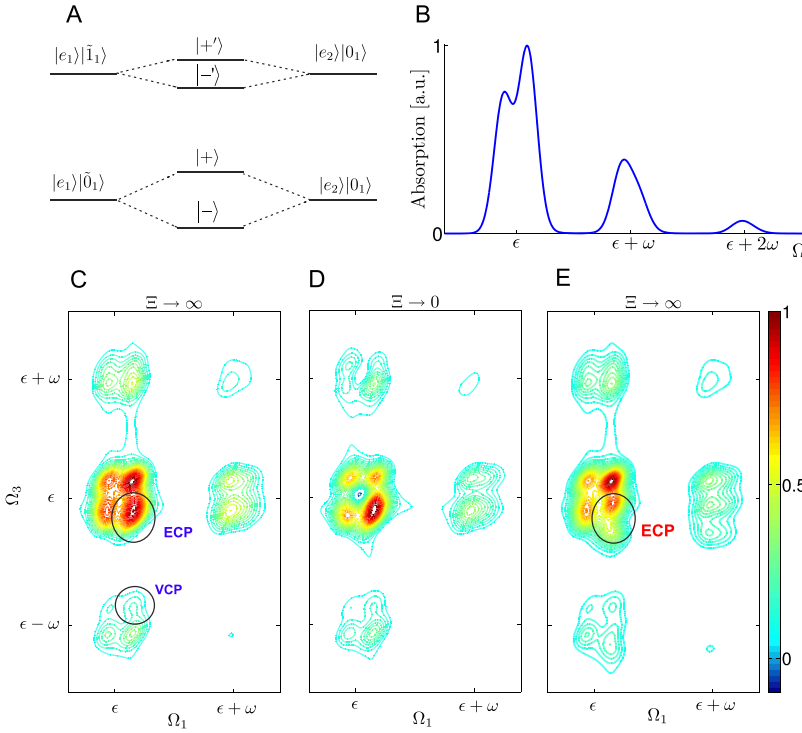
FIG. 5. Spectra of vibronic dimer, with parameters $\epsilon_1 = \epsilon_2$, $\mu_1/\mu_2 = 10$, $J_{12}/\omega = 1/8$, $\lambda_{\mathcal{A}} = 2J_{12}$, $\lambda_{\mathcal{A}}/\lambda_{\mathcal{V}} = 2$, $\lambda_{\mathcal{V}}/\Lambda_{\mathcal{V}} = 10$, $\Lambda_{\mathcal{V}}/\Lambda_{\mathcal{A}} = 10$, $\frac{\hbar\omega}{k_BT} = 26.7$, $\Lambda_{\mathcal{A}}t_2 = 0.65$, $\frac{m\omega^2 d^2}{4\hbar\omega} = 0.15$. (a) Level scheme of the $\mathbb{E}$ manifold. States $|+\rangle$ and $|-\rangle$ are symmetric and anti-symmetric combinations of the local states, respectively. (b) Absorption spectrum. (c) 2D spectrum with $\Xi_{12} \to \infty$ (i.e., Re $\sum_{n=1}^{4} S_n$) calculated using Eqs. (48) and (C1) at $t' = t_2/2$. (d) 2D spectrum Re $\sum_{n=1}^{6} S_n$ with $\Xi_{12} = 0$. (e) The same 2D spectrum as in (c), but with transport contributions approximated using Eq. (51).

$$\rho_{\text{eq},\alpha} = \frac{e^{-\hbar\varepsilon_\alpha/(k_BT)}}{\sum_{\alpha \in \mathbb{G}} e^{-\hbar\varepsilon_\alpha/(k_BT)}}. \qquad (41)$$

Inserting Eq. (40) into Eq. (39), we obtain a practical form of definition for phase factors

$$F_{\beta\alpha}^{(2)}(\tau_2, \tau_1) = \left\langle \mathcal{U}_\alpha(-\infty - \tau_2)\mathcal{U}_\beta(\tau_2 - \tau_1)\mathcal{U}_\alpha(\tau_1 + \infty) \right\rangle_B. \quad (42)$$

Equation (42) can be often simplified because the bath evolution in the initial state α is trivial in many realistic cases. For instance, $\hat{\Delta}_\alpha = 0$ holds for all $\alpha \in \mathbb{G}$ eigenstates for the standard excitonic $\hat{H}_{SB,E}$ and linear vibrational $\hat{H}_{SB,L}$ couplings. Then, by dropping trivial evolution in the α state, Eq. (42) can be evaluated exactly by using the second cumulant[22]

$$F_{\beta\alpha}^{(2)}(\tau_2, \tau_1)\big|_{\hat{\Delta}_\alpha = 0} = \exp(-g_{\beta\beta}(\tau_{21})), \qquad (43)$$

where $\tau_{ij} \equiv \tau_i - \tau_j$. Equation (43) shall be inserted into the linear response function [Eq. (38)] to complete the algorithm for calculating absorption lineshapes. Here we pay the debt of Sec. V: For a single chromophore with a single vibration, the eigenstates of $\mathbb{E}$ are the shifted vibrational states of Eq. (5), and at low temperatures ($\rho_{\text{eq},0} = 1$, $\hat{\Delta}_0 = 0$), Eqs. (38) and (43) simplify into Eq. (32) used to calculate lineshapes of Fig. 2.

The general estimate of Eq. (42) including account of the ground state to bath correlations (see Ref. 16 for an alternative notation) is relevant for many extensions of the standard vibronic model when $\hat{\Delta}_\alpha \neq 0$, e.g., for the quadratic system-bath coupling Eq. (12) at finite temperatures $\rho_{\text{eq},1} \neq 0$,

when the vibrations are anharmonic,[66] or when $\mathbb{G}$ and $\mathbb{F}$ manifolds are coupled.[67] Evaluated using the second cumulant, it reads as

$$\begin{aligned} F_{\beta\alpha}^{(2)}(\tau_2, \tau_1) = F_{\beta\alpha}^{(2)}(\tau_2, \tau_1)\big|_{\hat{\Delta}_\alpha = 0} \exp\big(&-g_{\alpha\alpha}(\tau_{21}) \\ &+ g_{\alpha\beta}(\tau_{21}) + g_{\beta\alpha}(\tau_{21}) + ir_{\alpha\alpha}\tau_{21} + ir_{\alpha\beta}\tau_{12}\big), \end{aligned}$$
$$(44)$$

where we employed the asymptotic form $2\,\text{Im}\left[g_{\alpha\beta}(t)\right] \approx r_{\alpha\beta}t$, where

$$\begin{aligned} r_{\alpha\beta} &\equiv \lim_{t\to\infty} \frac{2\,\text{Im}\left[g_{\alpha\beta}(t)\right]}{t} \\ &= 2\left(\sum_i \lambda_{\mathcal{A}}^i a_{\alpha\alpha}^i a_{\beta\beta}^i + \sum_{i,z} \lambda_{\mathcal{V}}^{i,z} v_{\alpha\alpha}^{i,z} v_{\beta\beta}^{i,z} + \sum_{i,z} \lambda_{\mathcal{W}}^{i,z} w_{\alpha\alpha}^{i,z} w_{\beta\beta}^{i,z}\right). \end{aligned}$$
$$(45)$$

We next turn to the third-order response and evaluate Eq. (35). The evolution superoperator $G(t)$ brings different bath factors $\mathcal{U}$ for transport [Eq. (37)] and dephasing [Eq. (36)] matrix elements and, consequently, the structure of bath factors different for pathways with and without transport during the t_2 interval. We thus partition the response function $S_1, \ldots, S_6$ to transfer S^O and non-transfer S^D pathways visualized in Fig. 3,

$$S_j(t_1, t_2, t_3) = S_j^D(t_1, t_2, t_3) + S_j^O(t_1, t_2, t_3). \qquad (46)$$

Expanding Eq. (35) in the vibronic index and merging phase factors, we get for the emission pathways

$$S_1^D(t_1, t_2, t_3) = \sum_{\alpha,\gamma \in \mathbb{G}} \sum_{\beta,\delta \in \mathbb{E}} \mu_{\gamma\beta}\mathcal{G}_{\beta\gamma,\beta\gamma}(t_3)\mu_{\delta\gamma}^\dagger \mathcal{G}_{\beta\delta,\beta\delta}(t_2)\mu_{\alpha\delta}\mathcal{G}_{\beta\alpha,\beta\alpha}(t_1)\mu_{\beta\alpha}^\dagger \rho_{\text{eq},\alpha} F_{\delta,\gamma,\beta,\alpha}^{(4)}(t_1, t_1 + t_2, t_1 + t_2 + t_3, 0),$$

$$S_2^D(t_1, t_2, t_3) = \sum_{\alpha,\gamma \in \mathbb{G}} \sum_{\beta,\delta \in \mathbb{E}} \mu_{\gamma\beta}\mathcal{G}_{\beta\gamma,\beta\gamma}(t_3)\mu_{\delta\gamma}^{\dagger}\mathcal{G}_{\beta\delta,\beta\delta}(t_2)\mu_{\beta\alpha}^{\dagger}\mathcal{G}_{\alpha\delta,\alpha\delta}(t_1)\mu_{\alpha\delta}\rho_{eq,\alpha}F_{\delta,\gamma,\beta,\alpha}^{(4)}(0, t_1 + t_2, t_1 + t_2 + t_3, t_1), \quad (47)$$

and

$$S_1^O(t_1, t_2, t_3) = \sum_{\substack{\alpha,\delta \in \mathbb{G} \\ }} \sum_{\substack{\beta,\gamma \in \mathbb{E} \\ \gamma \neq \beta}} \mu_{\delta\gamma}\mathcal{G}_{\gamma\delta,\gamma\delta}(t_3)\mu_{\gamma\delta}^{\dagger}\mathcal{G}_{\gamma\gamma,\beta\beta}(t_2)\mu_{\alpha\beta}\mathcal{G}_{\beta\alpha,\beta\alpha}(t_1)\mu_{\beta\alpha}^{\dagger}\rho_{eq,\alpha}F_{\beta,\gamma,\delta,\gamma,\beta,\alpha}^{(6)}(t_1, t_1 + t', t_1 + t_2, t_1 + t_2 + t_3, t_1 + t', 0),$$

$$S_2^O(t_1, t_2, t_3) = \sum_{\substack{\alpha,\delta \in \mathbb{G} \\ }} \sum_{\substack{\beta,\gamma \in \mathbb{E} \\ \beta \neq \gamma}} \mu_{\delta\gamma}\mathcal{G}_{\gamma\delta,\gamma\delta}(t_3)\mu_{\gamma\delta}^{\dagger}\mathcal{G}_{\gamma\gamma,\beta\beta}(t_2)\mu_{\beta\alpha}^{\dagger}\mathcal{G}_{\alpha\beta,\alpha\beta}(t_1)\mu_{\alpha\beta}\rho_{eq,\alpha}F_{\beta,\gamma,\delta,\gamma,\beta,\alpha}^{(6)}(0, t_1 + t', t_1 + t_2, t_1 + t_2 + t_3, t_1 + t', t_1).$$

$$(48)$$

Similar expansions of the ground state bleach, excited state absorption, and double quantum coherence pathways are summarized in Appendix C. The bath phase factors for non-transfer

$$F_{\delta,\gamma,\beta,\alpha}^{(4)}(\tau_4, \tau_3, \tau_2, \tau_1) = \left\langle \mathcal{U}_\alpha(-\infty - \tau_4)\mathcal{U}_\delta(\tau_{43})\mathcal{U}_\gamma(\tau_{32})\mathcal{U}_\beta(\tau_{21})\mathcal{U}_\alpha(\tau_1 + \infty) \right\rangle_B, \quad (49)$$

and transfer types of pathways

$$F_{\kappa,\eta,\delta,\gamma,\beta,\alpha}^{(6)}(\tau_6, \tau_5, \tau_4, \tau_3, \tau_2, \tau_1) = \left\langle U_\alpha(-\infty - \tau_6)U_\kappa(\tau_{65})U_\eta(\tau_{54})U_\delta(\tau_{43})U_\gamma(\tau_{32})U_\beta(\tau_{21})U_\alpha(\tau_1 + \infty) \right\rangle_B \quad (50)$$

are evaluated exactly using the second cumulant in Appendix D.

We next discuss the characteristic features of lineshapes prescribed by Eq. (50). First we plot lineshapes of a single emission pathway not complicated by complex interferences with bleach and ESA contributions. We consider transfer diagrams S_1^O and S_2^O of Fig. 3, starting and ending in the same ground state $\delta = \alpha$ and transferring the excitation between two vibronic eigenstates β to γ in the $\mathbb{E}$ manifold. For simplicity, we consider that the bath acts similarly on both states $a_{\gamma\gamma}^i = a_{\beta\beta}^i$. A combination of the rephasing and nonrephasing signals $S_1^O(\Omega_1, t_2, \Omega_3) + S_2^O(\Omega_1, t_2, \Omega_3)$ is shown in the top panels of Fig. 4 for three delay times t_2. At short delay times of the left panel, the peak is elongated but assumes to be more symmetric with increasing t_2, being simultaneously shifted down in frequencies Ω_3. A qualitatively similar behavior was reported for the principal peak,[68] and in full analogy, we can ascribe the elongation to the bath-induced correlations of transition frequency in periods t_1 and t_3 and the shift to bath reorganization. In Fig. 4(c), the peak-shape evolution is almost finished. In the bottom panels of Fig. 4, these changes were quantified and displayed as the functions of delay time. The shift is measured as the position of the peak maximum and plotted in Fig. 4(d) and the shape is characterized by the ratio of diagonal and anti-diagonal FWHM[69] in Fig. 4(e). Both panels show the transition from a static case of diagonal peaks with no shift into the symmetric, shifted lineshape. In contrast, both values would be constant in t_2 when phase acquisition during transport is ignored. In our simple example, transition has a character of exponential decay at the $1/\Lambda_A$ time scale. In a more sophisticated case, the bath would act differently at the vibronic states $a_{\gamma\gamma}^i \neq a_{\beta\beta}^i$ resulting in a complex multiexponential t_2 dynamics of shift and ellipticity, which would be also beyond the reach of approximations allowing the phase to follow t_2 evolution in a fixed vibronic state.

Lineshapes of emission diagrams shown in Fig. 4, disregarding bleach and ESA, are naturally related to the fluorescence excitation measurement.[70,71] Prospective accomplishment of its time-resolved variant at ultrafast time scales will provide a perfect case for our simulations. At the present state of experimental art, however, we have to rather address the standard 2D spectra related to differential absorption, where the emission is stimulated and its lineshapes always interfere with ground state bleach pathways S_3, S_4 and at times even with ESA S_5, S_6. To asses the effect of Eq. (48) on full 2D, we have calculated example 2D spectra of an excitonic dimer symmetric in energies $\epsilon_1 = \epsilon_2$ but with different dipoles $\mu_1/\mu_2 = 10$, allowing for spectroscopy of both symmetric and anti-symmetric excitons, and modulated by a single vibration residing at the first molecule, in the $J_{12} < \omega$ parametric regime.

The level structure is as follows: the ground state manifold $\mathbb{G}$ consists of vibrational states g, $g' \equiv |g\rangle|1_1\rangle$, ... The scheme [Fig. 5(a)] of the first excitonic manifold $\mathbb{E}$ suggests two levels around ϵ, $+$ and $-$ separated by effective resonant coupling $\tilde{J} \equiv J_{12}\langle 0|\tilde{0}\rangle$, and two levels, $+'$ and $-'$, around $\epsilon + \omega$, etc. The absorption line-shape [Fig. 5(b)] indeed shows two resolved peaks around ϵ; the doublet in vibronic progression is not resolved because the vibronic modulation reduces the effect of coupling. The existence of a doublet around $\varepsilon + \omega$ is only apparent in the peak asymmetry. Finally, $\mathbb{F}$ has vibrational states $f, f' \equiv |f\rangle|\tilde{1}_1\rangle$, ...

The 2D spectrum shows a rich structure of peaks, positions and magnitudes of which can be explained by combining the level structure, diagrams of Fig. 3, and transport dynamics of Eq. (15). Peak interferences are complex and very diverse in nature, e.g., the overlaps with ESA peaks strongly depend on the system specific double exciton shift Ξ_{12}. We show the overlap of emission and bleach [formally setting $\Xi_{12} \rightarrow \infty$, panel (c)] and further interference with ESA for $\Xi_{12} = 0$ in panel (d). Here, the peak structure of the (d) and (e) panels is the same, as for the $\Xi_{12} = 0$ case, the frequencies of $\mathbb{E} \rightarrow \mathbb{F}$ transitions correspond to frequencies of $\mathbb{G} \rightarrow \mathbb{E}$ transitions, e.g., $\varepsilon_f - \varepsilon_+ = \varepsilon_- - \varepsilon_g$, $\varepsilon_f - \varepsilon_- = \varepsilon_+ - \varepsilon_g$. However, when studied in detail, negative-going contributions of ESA affect the magnitude and shapes of peaks as will be discussed below. Magnitudes of emission, bleach, and ESA contributions to the
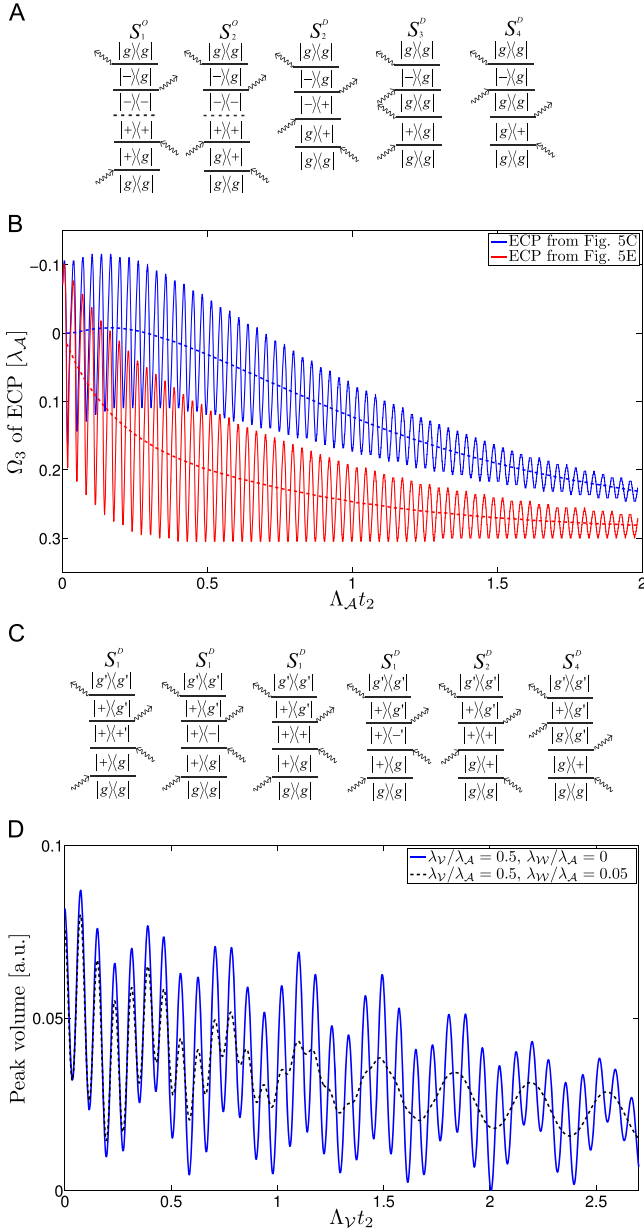
A

B

C

D

FIG. 6. (a) Feynman diagrams for the cross peaks ECP as marked in Figs. 5(c) and 5(d). Levels denoted according to Fig. 5(a). (b) Waiting time evolution of central detection frequency Ω_3 of ECP peaks for the calculation of Figs. 5(c) (blue) and 5(d) (red). Dotted lines average over a period of electronic beatings. Model and parameters as in Fig. 5(c). (c) Feynman diagrams for the cross peaks VCP as marked in Fig. 5(c). Levels denoted according to Fig. 5(a), g' is the first vibrational excitation $|g'\rangle \equiv |g\rangle |1_1\rangle$. (d) Modulation of the VCP [marked in Fig. 5(c)] peak. The blue line represents simulation with linear vibration-bath coupling parametrized as in Fig. 5(c). For the black line, quadratic vibration-bath coupling $\hat{H}_{SB,N}$ is added with parameters $\lambda_{\mathcal{W}} = 0.1\lambda_{\mathcal{V}}$, $\Lambda_{\mathcal{W}} = \Lambda_{\mathcal{V}}$.

four peaks of vibronic splitting around $(\epsilon \pm \tilde{J}, \epsilon \pm \tilde{J})$ are summarized in Table I, as obtained by evaluating relevant response functions for $t_1 = t_3 = 0$. Obviously the effect of ESA in Fig. 5(d) is disproportional: at low temperatures $\tilde{J} > kT$ (valid for parameters of Fig. 5), the peaks $\Omega_3 = \epsilon + \tilde{J}$ are significantly reduced by ESA as $\mathcal{G}_{--,--}(t_2) \approx 1$ and $\mathcal{G}_{--,++} \xrightarrow{t_2 \to \infty} 1$. On the contrary, $\mathcal{G}_{++,++} \xrightarrow{t_2 \to \infty} 0$ vanishes quickly and the lower peaks $\Omega_3 = \epsilon - \tilde{J}$ are thus less affected by ESA.

Such considerations are standard;[72] however, our algorithm aims at describing details of peak-shape evolution. We demonstrate it on a specific electronic cross peak ECP around $(\Omega_1, \Omega_3) \sim (\epsilon + \tilde{J}, \epsilon - \tilde{J})$ marked in Fig. 5(c). It is contributed by bleach pathway $\propto \mathcal{G}_{gg,gg}$, interfering with the emission pathways representing transport $|+\rangle \to |-\rangle$, $\propto \mathcal{G}_{--,++}$, along with some beating diagrams, all shown in Fig. 6(a) and eventually negative ESA contribution $\propto -\mathcal{G}_{++,++}$ for $\Xi_{12} = 0$ in Fig. 5(d). The bleach contribution is centered at stable (absorption) frequency $\Omega_3 = \epsilon - \tilde{J}$ and is constant in time $\mathcal{G}_{gg,gg}(t_2) = 1$. The emission (and eventually ESA) peak is progressively shifted down toward emission frequency $\delta\Omega_3 \propto -\mathrm{Im}\, \dot{g}(t_2)$. Its magnitude grows up as $\mathcal{G}_{--,++}(t_2) \approx 1 - e^{-R_{++,++}t_2}$ (for $T \to 0$), and eventually added ESA interpolates from a negative to positive peak $\mathcal{G}_{--,++}(t_2) - \mathcal{G}_{++,++}(t_2) \approx 1 - 2e^{-R_{++,++}t_2}$. Their overlap explains differences between ECP structures of Figs. 5(c) and 5(d). Shifted contribution is positive and larger in Fig. 5(c) and emphasizes lower Ω_3 frequencies of ECP compared to that of Fig. 5(d) reduced by ESA.

We next demonstrate the role of the phase factor $F^{(6)}$ and compare the lineshapes calculated by employing the full prescription of Eq. (48) in Fig. 5(c) ($\Xi_{12} = \infty$ case) with calculations implementing a much simpler $t_2 \to \infty$ limit of $F^{(6)}$ [Fig. 5(e)], which combines the factor $F^{(2)}$ for absorption in the t_1 interval with the factor $F^{(2)*}e^{ir t_3}$ for emission in t_3,

$$
\begin{aligned}
S_1^O(t_1, t_2, t_3) = \sum_{\substack{\alpha,\delta \in \mathbb{G} \\ \gamma \neq \beta}} \sum_{\beta,\gamma \in \mathbb{E}} & \mu_{\delta\gamma} \mathcal{G}_{\gamma\delta,\gamma\delta}(t_3) \mu_{\gamma\delta}^{\dagger} \mathcal{G}_{\gamma\gamma,\beta\beta}(t_2) \\
& \times \mu_{\alpha\beta} \mathcal{G}_{\beta\alpha,\beta\alpha}(t_1) \mu_{\beta\alpha}^{\dagger} \rho_{\mathrm{eq},\alpha} F_{\beta\alpha}^{(2)}(t_1, 0) \\
& \times F_{\gamma\delta}^{(2)*}(t_3, 0) e^{ir_{\gamma\gamma}t_3},
\end{aligned}
$$

$$
\begin{aligned}
S_2^O(t_1, t_2, t_3) = \sum_{\substack{\alpha,\delta \in \mathbb{G} \\ \beta \neq \gamma}} \sum_{\beta,\gamma \in \mathbb{E}} & \mu_{\delta\gamma} \mathcal{G}_{\gamma\delta,\gamma\delta}(t_3) \mu_{\gamma\delta}^{\dagger} \mathcal{G}_{\gamma\gamma,\beta\beta}(t_2) \\
& \times \mu_{\beta\alpha}^{\dagger} \mathcal{G}_{\alpha\beta,\alpha\beta}(t_1) \mu_{\alpha\beta} \rho_{\mathrm{eq},\alpha} F_{\beta\alpha}^{(2)}(0, t_1) \\
& \times F_{\gamma\delta}^{(2)*}(t_3, 0) e^{ir_{\gamma\gamma}t_3}. \quad (51)
\end{aligned}
$$

TABLE I. Magnitudes of four peaks around $(\epsilon \pm \tilde{J}, \epsilon \pm \tilde{J})$ as obtained by the analysis of Feynman diagrams. For simplicity, we assumed low temperatures so that $\mathcal{G}_{--,++} = 0$ and omitted rapidly oscillating terms $\propto \mathcal{G}_{-+,-+}, \mathcal{G}_{+-,+-}$ in the analysis.

Pathway \ peak	$(\epsilon - \tilde{J}, \epsilon + \tilde{J})$	$(\epsilon + \tilde{J}, \epsilon + \tilde{J})$	$(\epsilon - \tilde{J}, \epsilon - \tilde{J})$	$(\epsilon + \tilde{J}, \epsilon - \tilde{J})$
Emission	0	$\mu_{g+}^4 \mathcal{G}_{++,++}(t_2)$	$\mu_{g-}^4 \mathcal{G}_{--,--}(t_2)$	$\mu_{g+}^2 \mu_{g-}^2 \mathcal{G}_{--,++}(t_2)$
Bleach	$\mu_{g+}^2 \mu_{g-}^2 \mathcal{G}_{gg,gg}(t_2)$	$\mu_{g+}^4 \mathcal{G}_{gg,gg}(t_2)$	$\mu_{g-}^4 \mathcal{G}_{gg,gg}(t_2)$	$\mu_{g+}^2 \mu_{g-}^2 \mathcal{G}_{++,++}(t_2)$
ESA	$-\mu_{-f}^2 \mu_{g-}^2 \mathcal{G}_{--,--}(t_2)$	$-\mu_{g+}^2 \mu_{-f}^2 \mathcal{G}_{--,++}(t_2)$	0	$-\mu_{+f}^2 \mu_{g+}^2 \mathcal{G}_{++,++}(t_2)$

The two algorithms predict the same 2D lineshapes for short delays $t_2 = 0$ (not shown) before any transport can take place and S^D pathways dominate and also in the asymptotic region $t_2 \to \infty$ where the two prescriptions Eqs. (48) and (51) for S^O lineshapes agree. The differences appear at intermediate delay times shown in Figs. 5(c) and 5(e). The detection frequency Ω_3 of the emission pathway is lower (representing $t_2 \to \infty$ limit) for the approximation of Fig. 5(e); the parametrization of our example spectra shows up as an almost separated peak at the bottom of the ECP structure, while the overlap is smooth for the full calculation of Fig. 5(c). The difference in the waiting time evolution of ECP can be easily quantified for the detection frequency Ω_3 defined as the center of the mass of the ECP peak. It is shown in Fig. 6(b) as a function of delay time. Here, the periodic modulation represents electronic beatings [see the S_2^D diagram in Fig. 6(a)]. Averaging over the period (dashed lines) provides a smooth function accessible for explanation. Dynamics of the approximation is entirely induced by changing proportions of emission and bleaching contributions. In contrast, the shift of the "exact" result appears more slowly as the Stokes shift of the emission pathway is gradually developed during the t_2 period. The differences in peak-shape are rather complex, escaping some simple one-dimensional characterization. The ECP peak in 5(c) is less elongated along Ω_3 still as a result of developing Stokes shift of emission contribution. In addition, in the low frequency region, the emission pathways dominate and peak shapes are accordingly different here.

We next demonstrate the effects of the quadratic vibrational-bath coupling on the 2D spectrum. Both the effects of faster vibrational relaxation (Fig. 1) and widened peaks of progression (Fig. 2) are naturally present in the 2D spectrum as the width of 2D peaks and rate of vibrational relaxation. Beyond these effects, we have looked whether the vibrational dephasing introduced by quadratic coupling can be identified. We focused on the VCP vibronic cross peak, where the diagramatic analysis of Fig. 6(c) suggests the presence of vibronic beatings. In Fig. 6(d) we plotted the amplitude of the VCP peak as a function of delay. Interestingly we see two periodic modulations: a modulation with a shorter period $1/\omega$ represents vibrational coherence, while the slower period is of $|+\rangle\langle-|$ electronic origin. The two interfere to provide a complex beating pattern. The blue line represents the case of zero quadratic coupling, when both these oscillations survive for many periods. Increased quadratic coupling results in a selective decay of the vibrational coherence, as demonstrated by the black line that interpolates from complex, mixed coherence at short times to slower modulation of purely electronic coherence in the end of the time-window in Fig. 6(d). This is another demonstration of the decoherence effects of quadratic vibration to bath coupling, added to that in Sec. V. We note that the VCP peak is not significantly affected by ESA, and Fig. 6(c) represents the analysis of both $\Xi_{12} = 0$ and $\Xi_{12} \to \infty$ cases.

be reduced to formally similar computations. We have already reported vibronic calculations of transport times as deduced from transient grating measurements of kinetics of the artificial carotenoid-purpurin dyad[11] and natural lycopene-chlorophyll complex of Rs. molischianum.[10]

The present communication provides a detailed explanation on how we combine transport and dephasing dynamics into 2D lineshapes. We adopted an algorithm which, as compared to standard simulations, accounts for the phase-aquiring process along transport pathways and thus allows for accurate simulations of cross peak lineshapes, while not exceeding them in computational costs. Note that the 2D line-shape of the principal peak is widely used to study the spectral diffusion process.[68,69,73–77] With the present simulations, we are prepared to look at cross-peak-shapes with similar interest. The phase evolution during transport is most easily accessed when peaks of the transport pathways do not interfere with bleach and ESA peaks, as would be in the proposed measurements of time-resolved fluorescence excitation.[71]

The explicit representation of underdamped vibrations intrinsic to vibronic calculations opens the doors to relax standard assumptions of the spin-boson model for lineshapes at little additional computational cost. Here we made a step beyond the exponential decay of the Landau-Teller relaxation dynamics and employed quadratic damping to obtain subexponential vibrational relaxation. We analyzed all through the effects of such an extension for lineshapes of both absorption and 2D spectra. Note however that other extensions of the spin-boson dynamics model can be considered in the system part of the Hamiltonian. For example, we are not limited to harmonic profiles of vibrations linearly coupled to a chromophore. Realistic potential surfaces and nonlinear exciton to vibration coupling can be implemented. The study of anharmonic effects in 2D is in preparation[66] and shows certain similarities with the present calculations. Indeed, nonlinear transformations of coordinate or coupling are complementary strategies to generalize dynamics beyond the spin-boson case. The present model can thus also be used to account for certain dynamical aspects of anharmonic vibrations while avoiding notorious mathematical obstacles of higher polynomial potentials.

Another prospective generalization of the present simulations addresses the constant rates in time-local master equations [Eq. (15)]. Allowing time-dependent rates to account for transients of vibronic transport within the formalism of time-convolution-less master equations is an obvious idea, which fails, however, to resolve the true challenge connected with these transients: to account bath correlations between different periods of nonlinear response on transport.[78] Recently, a new type of projection formalism has been proposed that aims in this direction.[79] The perspective combination of this concept with the present algorithm for 2D lineshapes present seems to be a promising one.

VII. CONCLUSIONS

The present vibronic model was primarily designed to simulate the 2D-vis spectra for molecular dimers and for dyadic carotenoid-chlorophyll structures, where transport can

APPENDIX A: CORRELATED BATH

In the main text, we avoided various correlations that can arise between bath-induced motions. In this appendix, we cure this neglect. We adopt the following shorthand notation, where the three coupling matrices $a_{\alpha\beta}^i$, $v_{\alpha\beta}^{i,z}$, and $w_{\alpha\beta}^{i,z}$ are three components $\mathbf{y} = 1, 2, 3$ of general coupling $Y_{\alpha\beta}^{i,z,\mathbf{y}}$, i.e., $Y_{\alpha\beta}^{i,z,1} = \delta_{z0}a_{\alpha\beta}^i$, $Y_{\alpha\beta}^{i,z,2} = v_{\alpha\beta}^{i,z}$, and $Y_{\alpha\beta}^{i,z,3} = w_{\alpha\beta}^{i,z}$. Similarly the coupling constants are $\xi_{k,i,z}^{\mathbf{1}} = \iota_{k,i}\delta_{z0}$, $\xi_{k,i,z}^{\mathbf{2}} = \kappa_{k,i,z}$, and $\xi_{k,i,z}^{\mathbf{3}} = \zeta_{k,i,z}$. The system-bath Hamiltonian [Eq. (13)] has the form

$$\hat{H}_{SB} = \hbar \sum_{\alpha\beta,k} \sum_{i=1}^{N} \sum_{z=0}^{\infty} \sum_{\mathbf{y}=1}^{3} \Omega_k \left(\hat{B}_k Y_{\alpha\beta}^{i,z,\mathbf{y}} \xi_{k,i,z}^{\mathbf{y}} + h.c. \right) |\alpha\rangle \langle\beta|,$$

(A1)

where the index z formally runs over all non-negative integers assuming $Y_{\alpha\beta}^{i,0,2} = Y_{\alpha\beta}^{i,0,3} = 0$. We next define the general spectral density as

$$\mathcal{Y}_{i,z;i',z'}^{\mathbf{y},\mathbf{y}'}(x) \equiv \sum_k \Omega_k^2 \xi_{k,i,z}^{\mathbf{y}} \xi_{k,i',z'}^{\mathbf{y}'} \delta(x - \Omega_k).$$

(A2)

In the main text, we assumed the uncorrelated situation $\mathcal{Y}_{i,z;i',z'}^{\mathbf{y},\mathbf{y}'} \propto \delta_{\mathbf{y}\mathbf{y}'}\delta_{ii'}\delta_{zz'}$. Spectral densities of Eq. (20) are then recovered as $\mathcal{A}_i(x) = \mathcal{Y}_{i,0;i,0}^{1,1}(x)$, $\mathcal{V}_{i,z}(x) = \mathcal{Y}_{i,z;i,z}^{2,2}(x)$, and $\mathcal{W}_{i,z}(x) = \mathcal{Y}_{i,z;i,z}^{3,3}(x)$. The correlations between non-local (cross-chromophore) fluctuations are accounted by $i \neq i'$ terms, correlations between electronic-bath couplings and (quadratic) vibrational-bath couplings fluctuations relate to terms $\mathbf{y} \neq \mathbf{y}'$, and finally terms $z \neq z'$ account for the correlations between different vibrational modes.

In these general situations, the matrix of the correlation function Eq. (28) for diagonal noise

$$C_{\alpha\beta}''(\omega) = \sum_{\substack{i,i' \\ z,z' \\ \mathbf{y},\mathbf{y}'}} Y_{\alpha\alpha}^{i,z,\mathbf{y}} Y_{\beta\beta}^{i',z',\mathbf{y}'} \left[\mathcal{Y}_{i,z;i',z'}^{\mathbf{y},\mathbf{y}'}(\omega) - \mathcal{Y}_{i,z;i',z'}^{\mathbf{y},\mathbf{y}'}(-\omega) \right]$$

and rates for transport [Eq. (19)] for off-diagonal noise

$$R_{\nu\nu,\delta\delta} = -2 \sum_{i,i',z,z',\mathbf{y},\mathbf{y}'} \left\{ \mathcal{N}(\varepsilon_\nu - \varepsilon_\delta)\mathcal{Y}_{i,z;i',z'}^{\mathbf{y},\mathbf{y}'}(\varepsilon_\nu - \varepsilon_\delta) \right.$$
$$\left. + (\mathcal{N}(\varepsilon_\delta - \varepsilon_\nu) + 1)\mathcal{Y}_{i,z;i',z'}^{\mathbf{y},\mathbf{y}'}(\varepsilon_\delta - \varepsilon_\nu) \right\} Y_{\nu\delta}^{i,z,\mathbf{y}} Y_{\nu\delta}^{i',z',\mathbf{y}'}$$

(A3)

can be implemented keeping the rest of the algorithm unaffected.

APPENDIX B: LINE-SHAPE FUNCTION FOR OVERDAMPED SPECTRAL DENSITY

In this appendix, we specify the line-shape function $g_{\beta\alpha}(t)$ as defined by Eq. (31) for the overdamped spectral densities of Eqs. (20). To that end, we combine Eq. (29) with (31) and recall spectral densities $\mathcal{V}_{i,z}(\omega)$, $\mathcal{W}_{i,z}(\omega)$, $\mathcal{A}_{i,z}(\omega)$ of the overdamped Brownian oscillator [Eq. (20)]. For $t > 0$,

$$g_{\beta\alpha}(t) = g_{\beta\alpha}'(t) + ig_{\beta\alpha}''(t),$$

(B1)

where the imaginary part representing shifts is

$$g_{\beta\alpha}''(t) = -\sum_i a_{\alpha\alpha}^i a_{\beta\beta}^i \lambda_{\mathcal{A}}(e^{-\Lambda_{\mathcal{A}}^i t} + \Lambda_{\mathcal{A}}^i t - 1)/\Lambda_{\mathcal{A}}^i$$
$$- \sum_{i,z} v_{\alpha\alpha}^{i,z} v_{\beta\beta}^{i,z} \lambda_{\mathcal{V}}^{i,z}(e^{-\Lambda_{\mathcal{V}}^{i,z} t} + \Lambda_{\mathcal{V}}^{i,z} t - 1)/\Lambda_{\mathcal{V}}^{i,z}$$
$$- \sum_{i,z} w_{\alpha\alpha}^{i,z} w_{\beta\beta}^{i,z} \lambda_{\mathcal{W}}^{i,z}(e^{-\Lambda_{\mathcal{W}}^{i,z} t} + \Lambda_{\mathcal{W}}^{i,z} t - 1)/\Lambda_{\mathcal{W}}^{i,z}$$

(B2)

and the real part representing broadening is

$$g_{\beta\alpha}'(t) = \sum_i a_{\alpha\alpha}^i a_{\beta\beta}^i \lambda_{\mathcal{A}}^i \left\{ \coth\left(\frac{\hbar\Lambda_{\mathcal{A}}^i}{2k_BT}\right) \frac{e^{-\Lambda_{\mathcal{A}}^i t} + \Lambda_{\mathcal{A}}^i t - 1}{\Lambda_{\mathcal{A}}^i} + \frac{4\Lambda_{\mathcal{A}}^i k_BT}{\hbar} \sum_{n=1}^{\infty} \frac{e^{-\nu_n t} + \nu_n t - 1}{\nu_n(\nu_n^2 - \Lambda_{\mathcal{A}}^i \Lambda_{\mathcal{A}}^i)} \right\}$$
$$+ \sum_{i,z} v_{\alpha\alpha}^{i,z} v_{\beta\beta}^{i,z} \lambda_{\mathcal{V}}^{i,z} \left\{ \coth\left(\frac{\hbar\Lambda_{\mathcal{V}}^{i,z}}{2k_BT}\right) \frac{e^{-\Lambda_{\mathcal{V}}^{i,z} t} + \Lambda_{\mathcal{V}}^{i,z} t - 1}{\Lambda_{\mathcal{V}}^{i,z}} + \frac{4\Lambda_{\mathcal{V}}^{i,z} k_BT}{\hbar} \sum_{n=1}^{\infty} \frac{e^{-\nu_n t} + \nu_n t - 1}{\nu_n(\nu_n^2 - \Lambda_{\mathcal{V}}^{i,z} \Lambda_{\mathcal{V}}^{i,z})} \right\}$$
$$+ \sum_{i,z} w_{\alpha\alpha}^{i,z} w_{\beta\beta}^{i,z} \lambda_{\mathcal{W}}^{i,z} \left\{ \coth\left(\frac{\hbar\Lambda_{\mathcal{W}}^{i,z}}{2k_BT}\right) \frac{e^{-\Lambda_{\mathcal{W}}^{i,z} t} + \Lambda_{\mathcal{W}}^{i,z} t - 1}{\Lambda_{\mathcal{W}}^{i,z}} + \frac{4\Lambda_{\mathcal{W}}^{i,z} k_BT}{\hbar} \sum_{n=1}^{\infty} \frac{e^{-\nu_n t} + \nu_n t - 1}{\nu_n(\nu_n^2 - \Lambda_{\mathcal{W}}^{i,z} \Lambda_{\mathcal{W}}^{i,z})} \right\},$$

(B3)

where $\nu_n = \frac{2\pi n k_BT}{\hbar}$ are Matsubara frequencies. The line-shape function at negative times is eventually defined by the relation $g_{\beta\alpha}(-t) = g_{\beta\alpha}^*(t)$.

APPENDIX C: BLEACH, ESA, AND DOUBLE COHERENCE PATHWAYS

In this appendix, we expand the expressions for response functions of ground state bleach, excited state absorption, and double coherence pathways as represented in Fig. 3. The derivation is completely parallel to that of the emission pathways in Eq. (48) and yields

$$S_3^D(t_1, t_2, t_3) = \sum_{\alpha,\gamma \in \mathbb{G}} \sum_{\beta,\delta \in \mathbb{E}} \mu_{\alpha\delta} \mathcal{G}_{\delta\alpha,\delta\alpha}(t_3) \mu_{\delta\gamma}^\dagger \mathcal{G}_{\gamma\alpha,\gamma\alpha}(t_2) \mu_{\gamma\beta} \mathcal{G}_{\beta\alpha,\beta\alpha}(t_1) \mu_{\beta\alpha}^\dagger \rho_{eq,\alpha} F_{\delta,\gamma,\beta,\alpha}^{(4)}(t_1 + t_2 + t_3, t_1 + t_2, t_1, 0),$$

$$S_4^D(t_1, t_2, t_3) = \sum_{\alpha,\gamma \in \mathbb{G}} \sum_{\beta,\delta \in \mathbb{E}} \mu_{\gamma\beta} \mathcal{G}_{\beta\gamma,\beta\gamma}(t_3) \mu_{\beta\alpha}^\dagger \mathcal{G}_{\alpha\gamma,\alpha\gamma}(t_2) \mu_{\delta\gamma}^\dagger \mathcal{G}_{\alpha\delta,\alpha\delta}(t_1) \mu_{\alpha\delta} \rho_{eq,\alpha} F_{\delta,\gamma,\beta,\alpha}^{(4)}(0, t_1, t_1 + t_2 + t_3, t_1 + t_2),$$

$$S_5^D(t_1,t_2,t_3) = -\sum_{\alpha\in\mathbb{G}}\sum_{\beta,\delta\in\mathbb{E}}\sum_{\gamma\in\mathbb{F}}\mu_{\delta\gamma}\mathcal{G}_{\gamma\delta,\gamma\delta}(t_3)\mu_{\gamma\beta}^\dagger\mathcal{G}_{\beta\delta,\beta\delta}(t_2)\mu_{\alpha\delta}\mathcal{G}_{\beta\alpha,\beta\alpha}(t_1)\mu_{\beta\alpha}^\dagger\rho_{eq,\alpha}F_{\delta,\gamma,\beta,\alpha}^{(4)}(t_1,t_1+t_2+t_3,t_1+t_2,0),$$

$$S_6^D(t_1,t_2,t_3) = -\sum_{\alpha\in\mathbb{G}}\sum_{\beta,\delta\in\mathbb{E}}\sum_{\gamma\in\mathbb{F}}\mu_{\delta\gamma}\mathcal{G}_{\gamma\delta,\gamma\delta}(t_3)\mu_{\gamma\beta}^\dagger\mathcal{G}_{\beta\delta,\beta\delta}(t_2)\mu_{\beta\alpha}^\dagger\mathcal{G}_{\delta\alpha,\delta\alpha}(t_1)\mu_{\alpha\delta}\rho_{eq,\alpha}F_{\delta,\gamma,\beta,\alpha}^{(4)}(0,t_1+t_2+t_3,t_1+t_2,t_1),$$

$$S_7(t_1,t_2,t_3) = -\sum_{\alpha\in\mathbb{G}}\sum_{\beta,\delta\in\mathbb{E}}\sum_{\gamma\in\mathbb{F}}\mu_{\delta\gamma}\mathcal{G}_{\gamma\delta,\gamma\delta}(t_3)\mu_{\alpha\delta}\mathcal{G}_{\gamma\alpha,\gamma\alpha}(t_2)\mu_{\gamma\beta}^\dagger\mathcal{G}_{\beta\alpha,\beta\alpha}(t_1)\mu_{\beta\alpha}^\dagger\rho_{eq,\alpha}F_{\delta,\gamma,\beta,\alpha}^{(4)}(t_1+t_2,t_1+t_2,t_1,0),$$

$$S_8(t_1,t_2,t_3) = \sum_{\alpha\in\mathbb{G}}\sum_{\beta,\delta\in\mathbb{E}}\sum_{\gamma\in\mathbb{F}}\mu_{\alpha\delta}\mathcal{G}_{\delta\alpha,\delta\alpha}(t_3)\mu_{\delta\gamma}\mathcal{G}_{\gamma\alpha,\gamma\alpha}(t_2)\mu_{\gamma\beta}^\dagger\mathcal{G}_{\beta\alpha,\beta\alpha}(t_1)\mu_{\beta\alpha}^\dagger\rho_{eq,\alpha}F_{\delta,\gamma,\beta,\alpha}^{(4)}(t_1+t_2+t_3,t_1+t_2,t_1,0),$$

and, for transport pathways,

$$S_3^O(t_1,t_2,t_3) = \sum_{\substack{\alpha,\gamma\in\mathbb{G}\\ \alpha\neq\gamma}}\sum_{\beta,\delta\in\mathbb{E}}\mu_{\gamma\delta}\mathcal{G}_{\delta\gamma,\delta\gamma}(t_3)\mu_{\delta\gamma}^\dagger\mathcal{G}_{\gamma\gamma,\alpha\alpha}(t_2)\mu_{\alpha\beta}\mathcal{G}_{\beta\alpha,\beta\alpha}(t_1)\mu_{\beta\alpha}^\dagger\rho_{eq,\alpha}$$
$$\times F_{\gamma,\delta,\gamma,\alpha,\beta,\alpha}^{(6)}(t_1+t',t_1+t_2+t_3,t_1+t_2,t_1+t',t_1,0),$$

$$S_4^O(t_1,t_2,t_3) = \sum_{\substack{\alpha,\beta\in\mathbb{G}\\ \alpha\neq\beta}}\sum_{\gamma,\delta\in\mathbb{E}}\mu_{\beta\gamma}\mathcal{G}_{\gamma\beta,\gamma\beta}(t_3)\mu_{\gamma\beta}^\dagger\mathcal{G}_{\beta\beta,\alpha\alpha}(t_2)\mu_{\delta\alpha}^\dagger\mathcal{G}_{\alpha\delta,\alpha\delta}(t_1)\mu_{\alpha\delta}\rho_{eq,\alpha}$$
$$\times F_{\delta,\alpha,\beta,\gamma,\beta,\alpha}^{(6)}(0,t_1,t_1+t',t_1+t_2+t_3,t_1+t_2,t_1+t'),$$

$$S_5^O(t_1,t_2,t_3) = -\sum_{\alpha\in\mathbb{G}}\sum_{\substack{\beta,\gamma\in\mathbb{E}\\ \gamma\neq\beta}}\sum_{\delta\in\mathbb{F}}\mu_{\gamma\delta}\mathcal{G}_{\delta\gamma,\delta\gamma}(t_3)\mu_{\delta\gamma}^\dagger\mathcal{G}_{\gamma\gamma,\beta\beta}(t_2)\mu_{\alpha\beta}\mathcal{G}_{\beta\alpha,\beta\alpha}(t_1)\mu_{\beta\alpha}^\dagger\rho_{eq,\alpha}$$
$$\times F_{\beta,\gamma,\delta,\gamma,\beta,\alpha}^{(6)}(t_1,t_1+t',t_1+t_2+t_3,t_1+t_2,t_1+t',0),$$

$$S_6^O(t_1,t_2,t_3) = -\sum_{\alpha\in\mathbb{G}}\sum_{\substack{\beta,\gamma\in\mathbb{E}\\ \gamma\neq\beta}}\sum_{\delta\in\mathbb{F}}\mu_{\gamma\delta}\mathcal{G}_{\delta\gamma,\delta\gamma}(t_3)\mu_{\delta\gamma}^\dagger\mathcal{G}_{\gamma\gamma,\beta\beta}(t_2)\mu_{\beta\alpha}^\dagger\mathcal{G}_{\alpha\beta,\alpha\beta}(t_1)\mu_{\alpha\beta}\rho_{eq,\alpha}$$
$$\times F_{\beta,\gamma,\delta,\gamma,\beta,\alpha}^{(6)}(0,t_1+t',t_1+t_2+t_3,t_1+t_2,t_1+t',t_1). \tag{C1}$$

Expressions for S_3, S_4, S_5, and S_6 have been used for simulating 2D lineshapes in Figs. 5 and 6.

APPENDIX D: HIGHER PHASE FACTORS

In this appendix, we calculate the cumulative phase factors $F^{(4)}$ and $F^{(6)}$ [Eqs. (49) and (50)] for the third-order response functions. Using the same arguments as given above Eq. (43) for $F^{(2)}$, these higher functions can also be significantly simplified for the common case $\hat{\Delta}_\alpha = 0$. It can be figured out exactly for the Gaussian bath by using the second cumulant. After a bit of algebra, this yields

$$F_{\delta,\gamma,\beta,\alpha}^{(4)}(\tau_4,\tau_3,\tau_2,\tau_1)\Big|_{\hat{\Delta}_\alpha=0} = \exp\{-g_{\beta\beta}(\tau_{21})-g_{\gamma\gamma}(\tau_{32})-g_{\delta\delta}(\tau_{43})+g_{\beta\gamma}(\tau_{21})+g_{\beta\gamma}(\tau_{32})-g_{\beta\gamma}(\tau_{31})-g_{\beta\delta}(\tau_{32})$$
$$-g_{\beta\delta}(\tau_{41})+g_{\beta\delta}(\tau_{31})+g_{\beta\delta}(\tau_{42})+g_{\gamma\delta}(\tau_{32})+g_{\gamma\delta}(\tau_{43})-g_{\gamma\delta}(\tau_{42})\} \tag{D1}$$

and

$$F_{\kappa,\eta,\delta,\gamma,\beta,\alpha}^{(6)}(\tau_6,\tau_5,\tau_4,\tau_3,\tau_2,\tau_1)\Big|_{\hat{\Delta}_\alpha=0} = \exp\{-g_{\beta\beta}(\tau_{21})-g_{\gamma\gamma}(\tau_{32})-g_{\delta\delta}(\tau_{43})-g_{\eta\eta}(\tau_{54})-g_{\kappa\kappa}(\tau_{65})$$
$$-g_{\beta\gamma}(\tau_{31})+g_{\beta\gamma}(\tau_{32})+g_{\beta\gamma}(\tau_{21})-g_{\beta\delta}(\tau_{41})+g_{\beta\delta}(\tau_{42})+g_{\beta\delta}(\tau_{31})-g_{\beta\delta}(\tau_{32})-g_{\beta\eta}(\tau_{51})$$
$$+g_{\beta\eta}(\tau_{52})+g_{\beta\eta}(\tau_{41})-g_{\beta\eta}(\tau_{42})-g_{\beta\kappa}(\tau_{61})+g_{\beta\kappa}(\tau_{62})+g_{\beta\kappa}(\tau_{51})-g_{\beta\kappa}(\tau_{52})-g_{\gamma\delta}(\tau_{42})$$
$$+g_{\gamma\delta}(\tau_{43})+g_{\gamma\delta}(\tau_{32})-g_{\gamma\eta}(\tau_{52})+g_{\gamma\eta}(\tau_{53})+g_{\gamma\eta}(\tau_{42})-g_{\gamma\eta}(\tau_{43})-g_{\gamma\kappa}(\tau_{62})+g_{\gamma\kappa}(\tau_{63})$$
$$+g_{\gamma\kappa}(\tau_{52})-g_{\gamma\kappa}(\tau_{53})-g_{\delta\eta}(\tau_{53})+g_{\delta\eta}(\tau_{54})+g_{\delta\eta}(\tau_{43})-g_{\delta\kappa}(\tau_{63})+g_{\delta\kappa}(\tau_{64})+g_{\delta\kappa}(\tau_{53})$$
$$-g_{\delta\kappa}(\tau_{54})-g_{\eta\kappa}(\tau_{64})+g_{\eta\kappa}(\tau_{65})+g_{\eta\kappa}(\tau_{54})\}. \tag{D2}$$

The general form $\hat{\Delta}_\alpha \neq 0$ of $F^{(4)}$, $F^{(6)}$ requires adding corrections to Eq. (D2) for the initial state system-bath correlations as

$$F_{\delta,\gamma,\beta,\alpha}^{(4)}(\tau_4,\tau_3,\tau_2,\tau_1) = F_{\delta,\gamma,\beta,\alpha}^{(4)}(\tau_4,\tau_3,\tau_2,\tau_1)\Big|_{\hat{\Delta}_\alpha=0}\exp\{-g_{\alpha\alpha}(\tau_{41})+g_{\alpha\beta}(\tau_{21})+g_{\alpha\gamma}(\tau_{31})-g_{\alpha\gamma}(\tau_{21})$$
$$+g_{\alpha\delta}(\tau_{41})-g_{\alpha\delta}(\tau_{31})+g_{\beta\alpha}(\tau_{41})-g_{\beta\alpha}(\tau_{42})+g_{\gamma\alpha}(\tau_{42})-g_{\gamma\alpha}(\tau_{43})+g_{\delta\alpha}(\tau_{43})$$
$$+ir_{\alpha\beta}\tau_{12}+ir_{\alpha\gamma}\tau_{23}+ir_{\alpha\delta}\tau_{34}+ir_{\alpha\alpha}\tau_{41}\} \tag{D3}$$

and

$$
\begin{aligned}
F^{(6)}_{\kappa,\eta,\delta,\gamma,\beta,\alpha}(\tau_6, \tau_5, \tau_4, \tau_3, \tau_2, \tau_1) = \; & F^{(6)}_{\kappa,\eta,\delta,\gamma,\beta,\alpha}(\tau_6, \tau_5, \tau_4, \tau_3, \tau_2, \tau_1)\Big|_{\hat{\Delta}_\alpha = 0} \exp\{-g_{\alpha\alpha}(\tau_{61}) + g_{\alpha\beta}(\tau_{21}) + g_{\beta\alpha}(\tau_{61}) - g_{\beta\alpha}(\tau_{62}) \\
& + g_{\alpha\gamma}(\tau_{31}) - g_{\alpha\gamma}(\tau_{21}) + g_{\gamma\alpha}(\tau_{62}) - g_{\gamma\alpha}(\tau_{63}) + g_{\alpha\delta}(\tau_{41}) - g_{\alpha\delta}(\tau_{31}) + g_{\delta\alpha}(\tau_{63}) - g_{\delta\alpha}(\tau_{64}) \\
& + g_{\alpha\eta}(\tau_{51}) - g_{\alpha\eta}(\tau_{41}) + g_{\eta\alpha}(\tau_{64}) - g_{\eta\alpha}(\tau_{65}) + g_{\alpha\kappa}(\tau_{61}) - g_{\alpha\kappa}(\tau_{51}) + g_{\kappa\alpha}(\tau_{65}) + \mathrm{i}r_{\alpha\beta}(\tau_{12}) \\
& + \mathrm{i}r_{\alpha\gamma}\tau_{23} + \mathrm{i}r_{\alpha\delta}\tau_{34} + \mathrm{i}r_{\alpha\kappa}\tau_{45} + \mathrm{i}r_{\alpha\eta}\tau_{56} + \mathrm{i}r_{\alpha\alpha}\tau_{61}\}.
\end{aligned}
\tag{D4}
$$

These expressions should be inserted into Eqs. (48) to complete the simulation protocol.

[1]S. Mukamel, Annu. Rev. Phys. Chem. **51**, 691 (2000).
[2]D. M. Jonas, Annu. Rev. Phys. Chem. **54**, 425 (2003).
[3]M. Cho, *Two-Dimensional Optical Spectroscopy* (CRC Press, 2009).
[4]Y.-C. Cheng and G. R. Fleming, J. Phys. Chem. A **112**, 4254 (2008).
[5]V. Perlík, C. N. Lincoln, F. Šanda, and J. Hauer, J. Phys. Chem. Lett. **5**, 404 (2014).
[6]Th. Förster, Ann. Phys. **437**, 55 (1948).
[7]A. G. Redfield, IBM J. Res. Dev. **1**, 19 (1957).
[8]F. Terenziani and A. Painelli, Phys. Chem. Chem. Phys. **17**, 13074 (2015).
[9]D. Egorova, M. F. Gelin, and W. Domcke, Chem. Phys. **341**, 113 (2007).
[10]E. Thyrhaug, C. N. Lincoln, F. Branchi, G. Cerullo, V. Perlík, F. Šanda, H. Lokstein, and J. Hauer, "Carotenoid-to-bacteriochlorophyll energy transfer through vibronic coupling in LH₂ from *Phaeosprillum molischianum*," Photosynth. Res. (published online).
[11]V. Perlík, J. Seibt, L. J. Cranston, R. J. Cogdell, C. N. Lincoln, J. Savolainen, F. Šanda, T. Mančal, and J. Hauer, J. Chem. Phys. **142**, 212434 (2015).
[12]Y. Fujihashi, G. R. Fleming, and A. Ishizaki, J. Chem. Phys. **142**, 212403 (2015).
[13]M. H. Lee and A. Troisi, J. Chem. Phys. **146**, 075101 (2017).
[14]D. M. Monahan, L. Whaley-Mayda, A. Ishizaki, and G. R. Fleming, J. Chem. Phys. **143**, 065101 (2015).
[15]A. Chenu and G. D. Scholes, Annu. Rev. Phys. Chem. **66**, 69 (2015).
[16]W. M. Zhang, T. Meier, V. Chernyak, and S. Mukamel, J. Chem. Phys. **108**, 7763 (1998).
[17]J. Frenkel, Phys. Rev. **37**, 17 (1931).
[18]J. Frenkel, Phys. Rev. **37**, 1276 (1931).
[19]R. Peierls, Ann. Phys. **405**, 905 (1932).
[20]A. S. Davydov, *Theory of Molecular Excitons* (Springer, 1971).
[21]E. Silinsh and V. Čápek, *Organic Molecular Crystals: Interaction, Localization, and Transport Phenomena* (American Institute of Physics, 1994).
[22]V. Chernyak, F. Šanda, and S. Mukamel, Phys. Rev. E **73**, 036119 (2006).
[23]R. W. Zwanzig, *Lectures in Theoretical Physics* (Boulder, 1960), Vol. 3, p. 106.
[24]E. N. Zimanyi and R. J. Silbey, Philos. Trans. R. Soc., A **370**, 3620 (2012).
[25]F. C. Spano and S. Mukamel, Phys. Rev. A **40**, 5783 (1989).
[26]F. Šanda and S. Mukamel, J. Phys. Chem. B **112**, 14212 (2008).
[27]Y. Tanimura, J. Phys. Soc. Jpn. **75**, 082001 (2006).
[28]D. Abramavicius, B. Palmieri, D. V. Voronine, F. Šanda, and S. Mukamel, Chem. Rev. **109**, 2350 (2009).
[29]S. Mukamel and D. Abramavicius, Chem. Rev. **104**, 2073 (2004).
[30]C. Falvo, F. Šanda, and S. Mukamel, in *Ultrafast Infrared Vibrational Spectroscopy*, edited by M. D. Fayer (CRC Press, 2013), pp. 405–435.
[31]V. Butkus, L. Valkunas, and D. Abramavicius, J. Chem. Phys. **140**, 034306 (2014).
[32]V. Butkus, D. Zigmantas, D. Abramavicius, and L. Valkunas, Chem. Phys. Lett. **587**, 93 (2013).
[33]S. Polyutov, O. Kühn, and T. Pullerits, Chem. Phys. **394**, 21 (2012).
[34]M. Schröter, S. D. Ivanov, J. Schulze, S. P. Polyutov, Y. Yan, T. Pullerits, and O. Kühn, Phys. Rep. **567**, 1 (2015).
[35]H.-G. Duan, P. Nalbach, V. I. Prokhorenko, S. Mukamel, and M. Thorwart, New J. Phys. **17**, 072002 (2015).
[36]J. Wehner and V. Engel, Phys. Chem. Chem. Phys. **18**, 32910 (2016).
[37]A. Chenu, N. Christensson, H. F. Kauffmann, and T. Mančal, Sci. Rep. **3**, 2029 (2013).
[38]A. G. Dijkstra and Y. Tanimura, J. Chem. Phys. **142**, 212423 (2015).
[39]O. Flomenbom, K. Velonia, D. Loos, S. Masuo, M. Cotlet, Y. Engelborghs, J. Hofkens, A. E. Rowan, R. J. Nolte, M. Van der Auweraer, F. C. de Schryver, and J. Klafter, Proc. Natl. Acad. Sci. U. S. A. **102**, 2368 (2005).

[40]H. Yang, G. Luo, P. Karnchanaphanurach, T.-M. Louie, I. Rech, S. Cova, L. Xun, and X. S. Xie, Science **302**, 262 (2003).
[41]J. Klafter, M. F. Shlesinger, and G. Zumofen, Phys. Today **49**(2), 33 (1996).
[42]Y. Jung, E. Barkai, and R. J. Silbey, Chem. Phys. **284**, 181 (2002).
[43]G. Zumofen and J. Klafter, Chem. Phys. Lett. **219**, 303 (1994).
[44]S. C. Kou and X. S. Xie, Phys. Rev. Lett. **93**, 180603 (2004).
[45]F. Šanda and S. Mukamel, Phys. Rev. E **72**, 031108 (2005).
[46]G. Gangopadhyay and Y. Tanimura, Chem. Phys. Lett. **289**, 97 (1998).
[47]F. Šanda and S. Mukamel, Phys. Rev. E **73**, 011103 (2006).
[48]P. Allegrini, G. Aquino, P. Grigolini, L. Palatella, A. Rosa, and B. J. West, Phys. Rev. E **71**, 066109 (2005).
[49]A. Salam, *Molecular Quantum Electrodynamics: Long-Range Intermolecular Interactions* (John Wiley & Sons, 2010).
[50]B. P. Krueger, G. D. Scholes, and G. R. Fleming, J. Phys. Chem. B **102**, 5378 (1998).
[51]D. L. Andrews and T. Thirunamachandran, J. Chem. Phys. **67**, 5026 (1977).
[52]L. Landau and E. Teller, Phys. Z. Sowjetunion **10**, 34 (1936).
[53]E. E. Nikitin and J. Troe, Phys. Chem. Chem. Phys. **10**, 1483 (2008).
[54]S. Mukamel, *Principles of Nonlinear Optical Spectroscopy* (Oxford University Press, 1995).
[55]G. Lindblad, Commun. Math. Phys. **48**, 119 (1976).
[56]M. Tokuyama and H. Mori, Prog. Theor. Phys. **55**, 411 (1976).
[57]V. Čápek, Phys. A **203**, 520 (1994).
[58]P. N. Argyres and P. Kelley, Phys. Rev. **134**, A98 (1964).
[59]C. Olbrich and U. Kleinekathöfer, J. Phys. Chem. B **114**, 12427 (2010).
[60]A. O. Caldeira and A. J. Leggett, Phys. A **121**, 587 (1983).
[61]D. Abramavicius, L. Valkunas, and S. Mukamel, Europhys. Lett. **80**, 17005 (2007).
[62]J. Seibt and T. Pullerits, J. Chem. Phys. **141**, 114106 (2014).
[63]M. Yang and G. R. Fleming, J. Chem. Phys. **111**, 27 (1999).
[64]T. Mančal, J. Dostál, J. Pšenčík, and D. Zigmantas, Can. J. Chem. **92**, 135 (2013).
[65]M. Gell-Mann and F. Low, Phys. Rev. **84**, 350 (1951).
[66]A. Galestian Pour, C. N. Lincoln, V. Perlík, F. Šanda, and J. Hauer, "Anharmonic vibrations in linear and two-dimensional electronic spectra," Phys. Chem. Chem. Phys. (submitted).
[67]J. Seibt, V. Sláma, and T. Mančal, Chem. Phys. **481**, 218 (2016).
[68]F. Šanda, V. Perlík, C. N. Lincoln, and J. Hauer, J. Phys. Chem. A **119**, 10893 (2015).
[69]S. T. Roberts, J. J. Loparo, and A. Tokmakoff, J. Chem. Phys. **125**, 084502 (2006).
[70]H. Anzai, N. K. Joshi, M. Fuyuki, and A. Wada, Rev. Sci. Instrum. **86**, 014101 (2015).
[71]A. Perri, F. Preda, C. D'Andrea, E. Thyrhaug, G. Cerullo, D. Polli, and J. Hauer, Opt. Express **25**, A483 (2017).
[72]M. Cho, T. Brixner, I. Stiopkin, H. Vaswani, and G. R. Fleming, J. Chin. Chem. Soc. **53**, 15 (2006).
[73]K. Kwak, S. Park, I. J. Finkelstein, and M. D. Fayer, J. Chem. Phys. **127**, 124503 (2007).
[74]F. Šanda and S. Mukamel, Phys. Rev. Lett. **98**, 080603 (2007).
[75]K. Okumura, A. Tokmakoff, and Y. Tanimura, Chem. Phys. Lett. **314**, 488 (1999).
[76]C. Falvo, J. Chem. Phys. **144**, 234103 (2016).
[77]F. V. Camargo, H. L. Anderson, S. R. Meech, and I. A. Heisler, J. Phys. Chem. A **119**, 95 (2015).
[78]M. Richter and A. Knorr, Ann. Phys. **325**, 711 (2010).
[79]T. Mančal and F. Šanda, Chem. Phys. Lett. **530**, 140 (2012).